MACROGUIDE: TOPOLOGICAL GUIDANCE FOR MACROCYCLE GENERATION

Alicja Maksymiuk[1,2,†,*] **Alexandre Duplessis**[3,†] **Michael Bronstein**[1,2] **Alexander Tong**[2]
Fernanda Duarte[1] **İsmail İlkan Ceylan**[4,2]
[1]University of Oxford [2]AITHYRA [3]ENS Ulm [4]TU Wien

ABSTRACT

Macrocycles are ring-shaped molecules that offer a promising alternative to small-molecule drugs due to their enhanced selectivity and binding affinity against difficult targets. Despite their chemical value, they remain underexplored in generative modeling, likely owing to their scarcity in public datasets and the challenges of enforcing topological constraints in standard deep generative models. We introduce MACROGUIDE: Topological Guidance for Macrocycle Generation, a diffusion guidance mechanism that uses Persistent Homology to steer the sampling of pretrained molecular generative models toward the generation of macrocycles, in both unconditional and conditional (protein pocket) settings. At each denoising step, MACROGUIDE constructs a Vietoris-Rips complex from atomic positions and promotes ring formation by optimizing persistent homology features. Empirically, applying MACROGUIDE to pretrained diffusion models increases macrocycle generation rates from 1% to 99%, while matching or exceeding state-of-the-art performance on key quality metrics such as chemical validity, diversity, and PoseBusters checks.

1 INTRODUCTION

Macrocycles – cyclic molecules with a ring of 12 or more heavy atoms – have attracted growing interest as drug candidates due to their improved *selectivity* and *binding affinity* against difficult targets (Garcia Jimenez et al., 2023; Mallinson & Collins, 2012; Giordanetto & Kihlberg, 2014). The improvement in selectivity is largely attributed to the ring structure, which restricts molecular flexibility relative to linear analogs. This reduces off-target binding arising from conformational changes. Furthermore, macrocycles' larger size enables more protein-ligand interactions, allowing them to target challenging binding sites or even external protein surfaces (Yudin, 2015). The improvement in binding affinity comes from macrocycles' greater rigidity too, as it decreases their entropy in solvent and hence reduces entropic penalty upon binding.

Macrocycles in drug discovery. Many macrocycles can fold into conformations that mask polar groups (Naylor et al., 2017), which allows them to achieve oral bioavailability and to defy classical drug-likeness rules (e.g. Rule of 5 by Lipinski et al. (1997)). Macrocycles play a critical role in modern therapeutics with 17 macrocyclic drugs approved by the FDA in the last five years alone Du et al. (2025) (out of over 75 approved to date Jiang et al. (2026)). This includes clinical successes such as the immunosuppressant cyclosporine or the oncological drug lorlatinib (which outperforms its linear counterpart, crizotinib (Ermert, 2017; Shaw et al., 2020)). Despite these developments and the great therapeutic promise of macrocycles, they remain underexplored in deep generative modeling.

Macrocycle generation. Existing work on macrocycle[1] generation has mostly focused on cyclic peptides (see Appendix A.1 for a literature overview). These methods leverage peptide-specific traits, such as backbone homogeneity arising from a small set of amino-acid building blocks, which makes them inapplicable to structurally-diverse, arbitrary macrocycles.

[*]Corresponding author: `alicja.maksymiuk@cs.ox.ac.uk` [†]Equal contribution

[1]In this paper, *macrocycles* refer to molecules with a cycle of at least 12 heavy atoms, although this term is sometimes used to describe a specific subset of such molecules, namely *cyclic peptides*, which are built out of amino acids and peptide bonds.

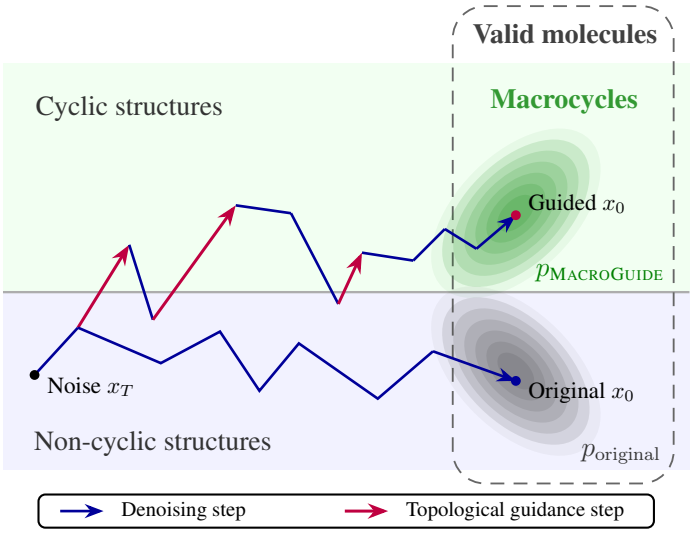

Figure 1: **Method overview.** MACROGUIDE drives the denoising trajectory towards macrocyclic structures using updates from a topological objective.

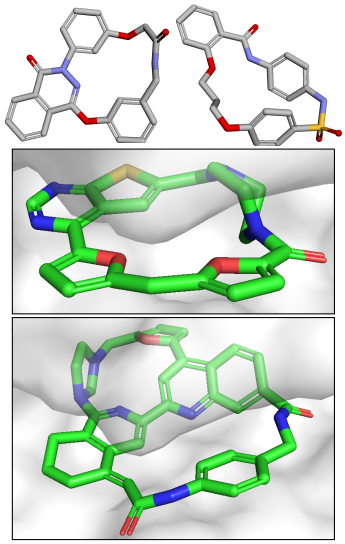

Figure 2: **Examples of generated macrocycles.** *Top:* Unconditional generation. *Middle:* Protein conditioning. *Bottom:* Specifically optimized to be bicyclic (two rings).

Non-peptidic macrocycle design has been explored in two prior works. Macformer, a SMILES-based transformer trained on linear-to-macrocyclic pairs, exploits the macrocyclization of pre-existing linear scaffolds to generate JAK2 inhibitors (Diao et al., 2023). Macro-Hop performs macrocycle scaffold hopping via reinforcement learning and successfully produces PDGFRα inhibitors by generating structures that satisfy predefined constraints and 3D similarity to a reference molecule (Liang et al., 2025). However, both methods rely on handcrafted scaffolds or linear precursors, which severely limits their applicability in *de novo* design, where neither the appropriate reference nor a linear equivalent is known *a priori*.

Problem statement and challenges. Despite the rapid progress of diffusion-based models for small-molecule design (Wang et al., 2025; Peng et al., 2023; Hoogeboom et al., 2022; Vignac et al., 2023a), to the best of our knowledge, *there is currently no generative method explicitly designed to produce arbitrary macrocycles*. This gap can be largely attributed to two factors. First, public chemical datasets contain relatively few macrocycles, often much simpler than therapeutically-relevant ones (Garcia Jimenez et al., 2023). Second, the existence of a large ring is a global topological property, whereas most generative models focus on approximating local chemical validity. As a result, existing unconstrained generative algorithms rarely produce macrocycles (see Table 1).

Contributions. We introduce Topological Guidance for Macrocycle Generation (MACROGUIDE), a diffusion guidance mechanism that steers pretrained molecular generative models – originally designed for unconstrained molecule generation – towards the generation of macrocycles, with or without conditioning (Figures 1 and 2). It works by computing gradients of the persistent homology features of a Vietoris-Rips complex at each step of the denoising process.

- Conceptually, MACROGUIDE is (i) *training-free*, generating macrocyclic topologies that may be rare or completely absent from the training data of the base model, without a need for retraining or finetuning; (ii) *lightweight*, introducing minimal computational overhead; (iii) *general*, as it can be plugged into various diffusion-based models; and (iv) *flexible*, allowing the user to specify both the number of rings and their sizes.
- Experimentally, we evaluate MACROGUIDE in both unconditional and conditional (protein pocket) settings; demonstrating a 99% rate of macrocycle generation, compared to a baseline of 0%-5%. Importantly, our method matches or exceeds state-of-the-art models across key quality metrics such as chemical validity, diversity, PoseBusters checks (Buttenschoen et al., 2024), and pharmacophore satisfaction.

This work introduces *the first de novo arbitrary macrocycle generation method*, addressing a critical gap in deep generative modeling for drug discovery.

2 PRELIMINARIES

2.1 DIFFUSION-BASED MOLECULE GENERATION

Diffusion models (Sohl-Dickstein et al., 2015; Ho et al., 2020; Song & Ermon, 2019) are a class of generative models that produce data by reversing a gradual noising process. In the forward process, a clean sample x_0 is progressively perturbed according to a Markov chain yielding noisy samples x_t that converge to an isotropic Gaussian as t increases. At the core of these models is the learning of the *score function*

$$\mathbf{s}_\theta(x_t, t) \approx \nabla_{x_t} \log p_t(x_t),$$

which estimates the gradient of the log-density of the perturbed data. It is then applied iteratively, starting from pure noise, to generate samples during the reverse process, also known as denoising (Song & Ermon, 2019; Song et al., 2021).

Diffusion models have been applied to tasks such as *de novo* molecule generation (Hoogeboom et al., 2022; Vignac et al., 2023a; Peng et al., 2023; Schneuing et al., 2024; Ziv et al., 2025; Schneuing et al., 2025), as their iterative denoising formulation allows models to capture global structural dependencies while refining fine-grained details. In the molecular setting, diffusion can either operate directly in continuous 3D coordinate space of atoms (Hoogeboom et al., 2022), on molecular graphs represented as adjacency matrices (Vignac et al., 2023a), or in a natural combination of both where the atom positions, atom types and bonds are included in the denoising network (Peng et al., 2023; Vignac et al., 2023b). In contrast to sequential (autoregressive) models, diffusion-based approaches can more easily generate molecules in their energetic minima without the need for further redocking, as they model the full joint distribution of atoms.

2.2 PERSISTENT HOMOLOGY FOR MOLECULAR POINT CLOUDS

Persistent homology is a tool from topological data analysis (TDA) that characterizes the topology of data across multiple scales (Edelsbrunner et al., 2002; Edelsbrunner & Harer, 2010). In the context of a molecular 3D point cloud, one constructs a family of *simplicial complexes* that encode proximity relationships between points, forming a nested sequence known as a *filtration*. A common choice is the *Vietoris-Rips complex* at scale ε:

$$\mathrm{VR}_\varepsilon(X) = \{\sigma \subseteq X \mid d(x_i, x_j) \leq \varepsilon; \forall\, x_i, x_j \in \sigma\},$$

where d is typically the Euclidean distance. As ε increases, the topology of $\mathrm{VR}_\varepsilon(X)$ evolves: connected components (captured by H_0) merge, loops and cycles (H_1) form and fill in, and in higher dimensions (H_2, etc.) voids appear and vanish. For each component $p_i^{(D)}$ of dimension D, persistent homology records the *birth* $b_i^{(D)}$ and *death* $d_i^{(D)}$ scales, producing a *persistence diagram* or *barcode*. In the context of molecules, H_0 features correspond to clusters of atoms, H_1 components often correspond to chemical rings or other cycle-like structures, and H_2 can capture internal cavities, relevant for instance in molecular cages. These descriptors are invariant to rigid transformations, robust to small perturbations and differentiable, making them useful for integrating topology information into various machine learning models (see Appendix A.2 for a literature overview).

3 METHODOLOGY

3.1 METHOD OVERVIEW

For each diffusion time step t, we define the state of a molecule as $M_t = \{X_t, A_t, B_t\}$, where $X_t \in \mathbb{R}^{N\times 3}$ describes the positions of the N atoms, $A_t \in [0,1]^{N\times a}$ is the probability distribution on their atomic types (with a the number of atom types), and $B_t \in [0,1]^{N\times N\times b}$ is the distribution on the bond types (if available), with b the number of allowed bond types, including the absence of a bond.

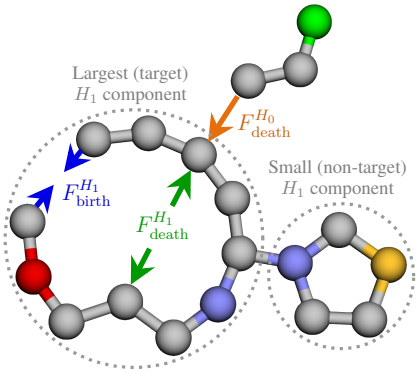

Figure 3: **Topological guidance.**

We update the score provided by the denoising architecture $s_\theta(X_t, t)$ with our guidance function $\mathcal{F}_{\mathrm{TDA}}$

$$\tilde{s}_\theta(X_t, t) = s_\theta(X_t, t) - \lambda_t \nabla_{X_t} \mathcal{F}_{\mathrm{TDA}}(X_t) \tag{1}$$

where λ_t allows for scheduling of the guidance.

The parameters of the original architecture remain fixed and the network is *not* retrained. The guidance term (Figure 3) is based on the computation of a Vietoris-Rips complex, and is defined as

$$\mathcal{F}_{\mathrm{TDA}}(X) = F^{H_1}_{\mathrm{death}}(X) + F^{H_1}_{\mathrm{birth}}(X) + F^{H_0}_{\mathrm{death}}(X) \tag{2}$$

- **Cycle size – H_1 death.** $F^{H_1}_{\mathrm{death}}$ encourages the size of the largest cycle to be in a given range. Specifically, we optimize $d^{(1)}_{i^\star}$ (where $i^\star = \arg\max_i d^{(1)}_i$), the death time of the H_1 component (ring) that dies last, to lie in a target interval $[d_{\min}, d_{\max}]$:

$$F^{H_1}_{\mathrm{death}}(X) = \Big(\mathrm{ReLU}\big(d_{\min} - d^{(1)}_{i^\star}(X)\big)\Big)^2 + \Big(\mathrm{ReLU}\big(d^{(1)}_{i^\star}(X) - d_{\max}\big)\Big)^2 \tag{3}$$

  This promotes the formation of a large cycle and enables control over its size. The link between the number of atoms in the cycle and the death time of its associated H_1 component is detailed in Section C.
- **Cycle connectivity – H_1 birth.** $F^{H_1}_{\mathrm{birth}}$ acts as a proxy for cycle connectivity, by ensuring each edge is not longer than the maximum allowed bond length $\ell^\star$. In practice

$$F^{H_1}_{\mathrm{birth}}(X) = \mathrm{ReLU}\big(b^{(1)}_{i^\star}(X) - \ell^\star\big) \tag{4}$$

  constrains the largest edge size in the cycle $b_{i^\star}$. Since bond information is not explicitly modeled, $F^{H_1}_{\mathrm{birth}}$ does not formally guarantee cycle connectivity, but we find it sufficient in practice. The absence of a squared penalty for this term, in contrast to the other guidance terms, empirically leads to improved performance (see Appendix J.3).
- **Molecule connectivity – H_0 death.** $F^{H_0}_{\mathrm{death}}$ promotes the existence of one single connected component by making sure all the distances between any two adjacent atoms (i.e. the death $d^{(0)}_j$ of an H_0 component) are of length less than the maximum allowed bond length $\ell^\star$:

$$F^{H_0}_{\mathrm{death}}(X) = \sum_{j=1}^{N_0} \Big(\mathrm{ReLU}\big(d^{(0)}_j(X) - \ell^\star\big)\Big)^2 \tag{5}$$

  where N_0 is the number of finite-death H_0 components.

Detailed algorithms can be found in Appendix F.

Addressing gradient sparsity. Each topological feature is created and destroyed by specific simplices. As a consequence, the gradient signal comes only from the few points involved in critical birth and death events (Poulenard et al., 2018). Although this is generally not problematic, as the critical points typically change across denoising steps (Carrière et al., 2021), it can render the optimization of H_0 components unstable and potentially divergent. We address this issue by masking the gradient of the atom closest to the molecular centroid. Further details and theoretical guarantees are provided in Appendix D.

3.2 Posterior Sampling

Following Guo et al. (2024), the score of a conditional distribution admits the decomposition

$$\nabla_x \log p_t(x \mid y) = \nabla_x \log p_t(x) + \nabla_x \log p_t(y \mid x).$$

In our setting, the guidance term can thus be interpreted as a conditional score term

$$\nabla_x \log p_t(y \mid x) = -\lambda_t \, \nabla_x \mathcal{F}_{\mathrm{TDA}}(x), \qquad \lambda > 0, \tag{6}$$

which corresponds to an energy-based conditional likelihood

$$p(y \mid x) \;\propto\; \exp\big(-\lambda_t \, \mathcal{F}_{\mathrm{TDA}}(x)\big).$$

Table 1: **Performance of unconditional macrocycle generation.** Results obtained from 1000 molecules with 30 heavy atoms.

Metrics (↑; [0-1])	MolDiff (no guid.)	MolDiff (finetuned)	Naive (12 atoms)	Naive (14 atoms)	Torus noise initialization	MolDiff+MACROGUIDE (ours)
Validity	0.991	**0.994**	0.937	0.930	0.993	0.989
Connectivity	0.958	0.993	0.985	0.990	0.960	**0.999**
Successfulness	0.949	0.987	0.923	0.921	0.953	**0.988**
Out of successful:						
Macrocycles	0.053	0.851	0.370	0.364	0.054	**0.997**

Table 2: **Performance of macrocycle generation with protein conditioning.**

Metrics (↑; [0-1])	MolSnapper (no guid.)	MolSnapper (finetuned)	Naive (12 atoms)	Naive (14 atoms)	MolSnapper+MACROGUIDE (ours)
Validity	0.858	0.795	0.819	0.791	**0.925**
Connectivity	1.000	1.000	1.000	1.000	1.000
Successfulness	0.858	0.795	0.819	0.791	**0.925**
Out of successful:					
Macrocycles	0.003	0.180	0.013	0.000	**0.995**

In particular Bayes' Theorem gives

$$p_t(x \mid y) \;\propto\; p_t(x)\exp\big(-\lambda_t\,\mathcal{F}_{\mathrm{TDA}}(x)\big),$$

and guidance can be interpreted as approximating sampling from this conditional distribution in the continuous-time limit with an exact score.

In practice, however, this interpretation only holds approximately. First, the learned score is imperfect, so the dynamics do not exactly track the target SDE. Gao et al. (2025) analyze this discrepancy and propose rectified guidance formulations to reduce bias from score errors. Second, practical samplers discretize the SDE. Guo et al. (2024) show that discretization introduces systematic deviations in the effective distribution, and propose variance-preserving corrections. Nevertheless, we find this approximation sufficient for our task, as shown in Section 4.

4 EXPERIMENTS

4.1 MAIN RESULTS

4.1.1 UNCONDITIONAL GENERATION

To demonstrate the ability of MACROGUIDE to generate macrocycles we apply it to MolDiff, a diffusion model that generates molecules by denoising a 3D point cloud of atoms, together with bonds (Peng et al., 2023). MolDiff was pretrained on GEOM-Drug (Axelrod & Gomez-Bombarelli, 2022), a dataset of small molecules with drug-like properties, where only 0.14% of the training data are macrocycles. In our guidance method, the simplicial complex is built using Pytorch Topological (Rieck, 2022). Further setup details are described in Appendix G.

Baselines. As MACROGUIDE is the first arbitrary macrocycle generation method, we cannot rely on established baselines. Instead, we design the following custom baselines. First, we evaluate whether macrocycles can be generated by **finetuning** existing models on macrocyclic datasets (Appendix H.1). Second, we construct a **naive** guidance mechanism that forces a chosen subset of atoms to form a ring, where adjacent atoms are kept close and opposite atoms are pushed apart (Appendix H.2). We check the performance for subset sizes of 12 and 14 atoms. Finally, we test whether initializing the denoising process with **torus-shaped noise** resembling a macrocycle improves generation (Appendix H.3).

Metrics. For consistency with previous approaches (Peng et al., 2023), we reuse the following metric definitions: molecules are considered **valid** if they can be parsed by RDKit (Landrum, 2013), **connected** if they have only one graph connected component, and **successful** if they meet both properties at the same time. If the generated molecule is successful, we test if the molecule is a **macrocycle** by checking for the presence of a chordless cycle of size at least 12 using `Chem.GetSymmSSSR`

from RDKit. This only includes cycles without edges between non-neighboring vertices, which excludes fused small rings where the outer boundary can have ≥ 12 atoms.

Parameter choice. During the experiments, we set $\lambda_t = 1$, $[d_{\min}, d_{\max}] = [4.45\ \text{Å}, 5.05\ \text{Å}]$, and $\ell^\star = 2\,\text{Å}$, which is chosen based on chemical knowledge and is slightly higher than longest common bonds in organic chemistry.

Results. Table 1 demonstrates that MACROGUIDE increases the number of generated macrocycles by almost 20-fold compared to MolDiff, and outperforms all the other baselines. Finetuning does yield a respectable generation rate, although generating about 15% fewer macrocycles than MACROGUIDE. Visualizations of generated molecules are provided in Appendix I.1.

4.1.2 PROTEIN CONDITIONING

MACROGUIDE can also be applied to molecular generation models conditioned on proteins which we demonstrate by guiding MolSnapper (Ziv et al., 2025). MolSnapper requires specifying the protein pocket placement and choosing a few atoms from a reference ligand to act as a pharmacophore. We follow the setup provided by the original work: we use the same protein pocket and choose reference atoms to guide generation within the protein. We reuse the same parameters as in Section 4.1.1. Further setup details are described in Appendix G.2.

Baselines. For comparison, we include the same baselines as in Section 4.1.1, albeit without the torus noise initialization because of its poor performance in the unconditional setting and because of the non-triviality of choosing the right placement and angle of the initial macrocycle-like noise.

Results. We report performance in Table 2. Similarly to the unconditional setting, the macrocycle generation rate increases from 0.3% to nearly 100%, representing a 300-fold increase. Importantly, MACROGUIDE is the only efficient method, as all of the baselines exhibit a dramatic performance drop. In particular, the performance of the finetuned model drops to 18%. This collapse can be attributed to the protein constraints pushing the finetuned model outside of its training distribution, leaving no explicit mechanism to constrain the trajectory back towards macrocyclic topologies. Consequently, we do not consider finetuning to be a robust solution for this task and do not assess it further. Visualizations of generated molecules are provided in Appendix I.2.

4.1.3 ASSESSING MACROCYCLE QUALITY

To further assess the quality of the macrocycles generated with MACROGUIDE we evaluate the following additional criteria: **novelty**, indicating whether a molecule is absent from the training dataset of the original model; **uniqueness**, measuring whether it differs from all the other generated samples; and **diversity**, assessed via fingerprint similarity across all pairs of generated molecules (Peng et al., 2023). Finally, to assess the chemical quality of the generated macrocycles we run **PoseBusters metrics** Buttenschoen et al. (2024) and report the fraction of molecules that pass all tests, as well as the performance for individual checks.

Conditional metrics. For conditional generation we also calculate PoseBusters metrics related to the protein. Additionally, **pharmacophore satisfaction** is evaluated by matching each reference atom to the closest atom in the generated molecule. A match is valid if the atom types agree and the distance is within 1 Å (Ziv et al., 2025). A pharmacophore is considered satisfied if at least 80% of the reference atoms are matched. Finally, we assess whether the generated molecules are likely to be orally available. Although there are no clearly established **Lipinski rules for macrocycles**, we follow Garcia Jimenez et al. (2023) and Viarengo-Baker et al. (2021) to propose the following rules: Molecular Weight (MW) < 1000 Da, number of Hydrogen Bond Donors (HBD) ≤ 7 and lipophilicity between 2.4 and 6, and we report the fraction of macrocycles meeting all of the criteria.

Results. Table 3 summarize the quality metrics of the generated macrocycles, with standard deviations reported in Appendix J.1. MACROGUIDE substantially outperforms the base model for most of the tested metrics, both in the unconditional and conditional settings. Additionally, our protein-conditioned macrocycles exhibit an important improvement in the internal energy test, which checks pose deviation from the relaxed molecule conformation. This suggests that MACROGUIDE addresses one of the prominent challenges in protein-conditioned molecular design: generated molecules are often not in their energetic minimum, resulting in low binding affinities and changes in

Table 3: **Unconditional and protein-conditioned macrocycle quality metrics.** Values were obtained by generating molecules until at least 1000 macrocycles were found to ensure reliable and comparable estimates. Some metrics are not reported because they are only defined in the presence of protein.

Metrics (↑; [0-1])	MolDiff (no guid.)	+MACROGUIDE (ours)	MolSnapper (no guid.)	+MACROGUIDE (ours)
Diversity	0.707	**0.771**	0.626	**0.712**
Novelty	1.000	1.000	1.000	1.000
Uniqueness	1.000	1.000	1.000	1.000
All PoseBusters tests	-	-	0.440	**0.575**
Ligand PoseBusters	0.663	**0.805**	0.539	**0.626**
Bond lengths	0.977	**0.990**	0.844	**0.860**
Bond angles	0.949	**0.987**	**0.913**	0.888
Internal steric clash	0.722	**0.844**	**0.862**	0.854
Aromatic ring flatness	0.980	**0.999**	**0.996**	0.992
Non-ar. ring non-flatness	0.981	**0.999**	0.993	**0.999**
Double bond flatness	0.965	**0.989**	0.980	**0.993**
Internal energy	0.961	**0.984**	0.818	**0.921**
Protein PoseBusters	-	-	0.806	**0.911**
Protein-ligand max. distance	-	-	1.000	1.000
Min. distance to protein	-	-	0.806	**0.907**
Volume overlap with protein	-	-	1.000	1.000
Pharmacophore satisfaction	-	-	0.769	**0.789**
Macrocycle Lipinski	-	-	0.551	**0.638**

pose after redocking (Harris et al., 2023). Finally, we observe an increase in the rate of pharmacophore satisfaction and compliance with Lipinski rules for macrocycles.

Furthermore, we examine atom type and ring size distributions of generated molecules, and show that MACROGUIDE preserves molecule complexity during macrocycle generation (Appendix J.5 and J.6). We also show that MACROGUIDE macrocycles tend to have fewer small strained rings, whose presence often poses a synthetic challenge.

Discussion. Notably, MACROGUIDE does not explicitly guide towards better 3D structure or molecular properties. The observed improvement in generative metrics possibly stems from the fact that MACROGUIDE fixes the global shape of the molecule at early stages of the denoising process, which allows the denoiser to spend more time refining the local structure of the molecule (see Figure 7). In contrast, without guidance the macrocycles represent a deviation from the training distribution, and likely assume cyclical shapes only later during the generation process.

4.2 ADDITIONAL MACROGUIDE APPLICATIONS

4.2.1 BICYCLIC MOLECULE GENERATION

Macrocycles can achieve better selectivity than small molecules, but as the ring grows, so does the conformational space of macrocycles, potentially allowing for off-target interactions. One way to generate larger binders without reducing selectivity is to generate bicyclic compounds Heinis et al. (2009); Rowland et al. (2025). To generate bicycles, we modify the topological guidance to optimize the two largest H_1 components, and we keep the same desired death time range. In Table 4 we show 97% and 90% bicyclic performance rates in the unconditional and conditional setups respectively. An example of a generated bicyclic molecule is shown in Figure 2.

Table 4: **Performance of bicyclic molecule generation in unconditional and conditional settings.** A molecule is considered bicyclic if it has at least two chordless cycles of at least 12 atoms each. Results obtained from 1000 molecules with 45 heavy atoms.

Metrics (↑; [0-1])	MolDiff +MACROGUIDE	MolSnapper +MACROGUIDE
Validity	0.998	0.821
Connectivity	0.931	1.000
Successfulness	0.929	0.821
Out of successful:		
Bicyclic molecule	0.970	0.895

4.2.2 H_0 DEATH GUIDANCE IMPROVES LARGE MOLECULE GENERATION

While originally designed as a stability safeguard for our guidance method, ablation studies reveal that H_0 death optimization improves large molecule generation beyond the macrocycle task. Notably, existing methods struggle with the generation of large molecular structures (Le et al., 2024) and often produce several disconnected components.

We show that it is possible to preserve molecule connectivity as the number of atoms increases, by applying our H_0 death optimization (Equation (5) with the gradient masking detailed in Appendix D). The results in Figure 4 show a drastic improvement in connectivity (80% versus 20% for $n = 110$). H_0 optimization therefore appears as an attractive sampling-time guidance method when dealing with large molecules.

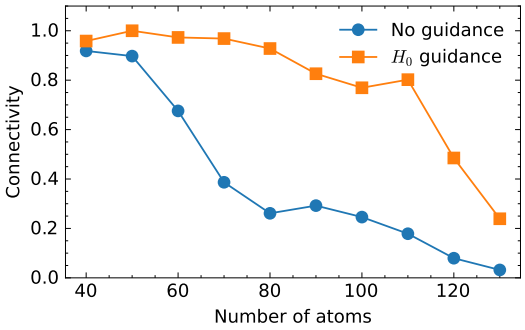

Figure 4: **Performance of MolDiff with increasing molecular size.** Adding H_0 guidance term improves performance for large molecule sizes. Results obtained from 200 samples each.

4.3 FURTHER ANALYSIS

4.3.1 MACROCYCLE SIZE CONTROL

A theoretical formula of the number of atoms in the cycle as a function of its topological death is derived in Appendix C. Figure 5 confirms the validity of the provided control equation, although we observe a slight underestimation of the actual values by the theoretical predictions. One possible explanation is that elongated elliptic rings have a lower death time than circular rings with the same number of atoms (see Figure 9b of Appendix D for a visualization).

Results are computed for 200 samples of 30 heavy atoms, with each target size $d^\star$ being constrained in the relaxed form of an interval $[d^\star - 0.05, d^\star + 0.05]$, sampled at 0.1 intervals.

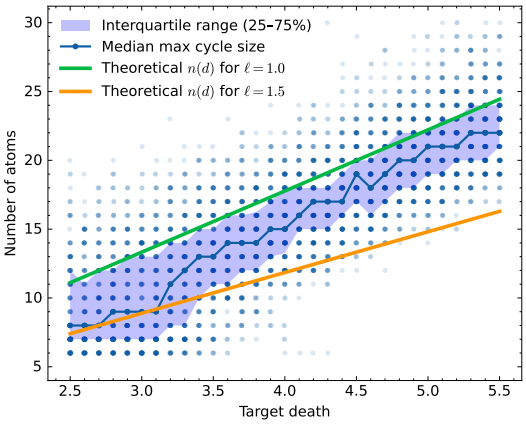

Figure 5: **Median max cycle size as a function of the target death.**

4.3.2 RUNTIME COMPARISON

Importantly, MACROGUIDE introduces only a very moderate computational overhead on top of the base denoising process. Figure 6 provides a breakdown of the average time per denoising step for MolSnapper ($\approx 17ms$) and MACROGUIDE ($\approx 21ms$). The extra cost of our guidance method is dominated by the computation of the Vietoris-Rips complex, which grows quadratically with n. This is reasonable since the denoising process is quadratic too and MACROGUIDE represents only 20% of the total cost. Nevertheless, we explored two different strategies to accelerate our guidance method. Both methods rely on selecting only a subset of the denoising steps to apply the guidance function.

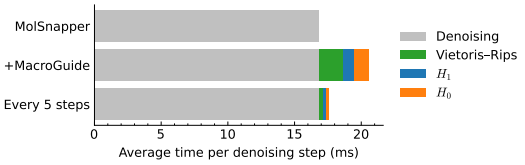

Figure 6: **Runtime comparison.** MACROGUIDE produces only a small computational overhead that can be further reduced by applying guidance only every k steps.

Guidance every k steps. Our first strategy consists of applying the topological guidance only once every k denoising steps, instead of at every step. Results for $k = 2, 3, 4, 5$ are reported in Appendix J.7.1. Importantly, we are able to divide the additional cost of MACROGUIDE by at least 5 with less than 15% degradation in macrocycle generation rates and molecular quality metrics relative

to full guidance. Notably, it also improves the rate of pharmacophore satisfaction, compared both to MolSnapper and MACROGUIDE with $k = 1$. This trade-off makes sparse guidance an attractive default choice in practice.

Late-start guidance. A second strategy we investigated consists of activating the topological guidance only during the later stages of the diffusion process. In practice, however, this approach consistently underperformed the previous strategy, which can be explained by the fact that noising processes tend to corrupt high-frequency information first (Falck et al., 2025), which means the shape of a molecule is likely decided early during denoising. For completeness, we report the corresponding results in Appendix J.7.2.

Consequently, applying guidance every k steps appears to be a good practical choice when trying to sample a handful of molecules, or when using high values of n.

4.3.3 STABILITY ANALYSIS

The considerable sparsity of gradients may cast doubt on the stability of the method. That is why we provide insights about the guidance process by tracking optimized topological features and their gradients throughout denoising. Full results and discussion can be found in Appendix E. In particular Figure 7 demonstrates the stability of MACROGUIDE, after as few as 100 denoising steps. More importantly, it provides an explanation to the success of our method: guidance shapes macrocyclic structure early, while late-stage denoising (last 200 steps) performs fine-grained chemical validity optimization without interference.

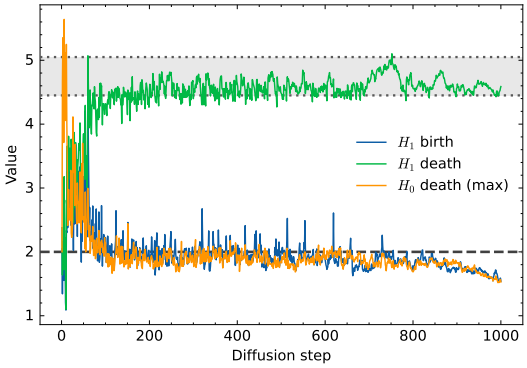

Figure 7: **Key topological features throughout denoising**. Maximum H_0 death (i.e. the longest distance to the closest neighbor over all atoms), and birth and death of the maximum-death H_1 component (largest cycle).

4.4 ABLATIONS

We further analyze the contribution of the different components of our guidance mechanism through a series of ablations. In Appendix J.2, we remove individual terms of the guidance function and show that all components are necessary in the unconditional setting. In the conditional setting, however, the H_0 death term (molecule connectivity) can be omitted, as the confined volume of the protein pocket naturally prevents atom disconnection. In Appendix J.3, we investigate how adding or removing the square of the topological terms influences performance. Finally, we study the sensitivity to guidance strength motivating the chosen value (Appendix J.4).

5 CONCLUSION

In this work, we presented MACROGUIDE, the first diffusion-based framework designed to generate arbitrary macrocycles without the need for model retraining or specialized datasets. By leveraging persistent homology to guide pretrained models, our method successfully bridges the gap between local chemical validity and global topological constraints. Specifically, our method drives the denoising path to a stable region of the set of cyclic structures, where validity optimization can be performed during later steps without interference from the guidance terms.

Experimentally, MACROGUIDE achieves a 99% macrocycle generation rate in both unconditional and protein-conditioned settings. Furthermore, the resulting molecules demonstrate superior 3D structural quality, exceeding or matching state-of-the-art performance on chemical validity, diversity, and PoseBusters benchmarks.

By providing a lightweight and training-free mechanism, MACROGUIDE offers a robust solution for exploring the macrocyclic chemical space. We provide a detailed discussion of promising future directions in Appendix B. We anticipate that this framework will integrate naturally with the expanding class of 3D point-cloud-based models, allowing topological guidance to contribute to continued improvements in generative drug discovery.

ACKNOWLEDGMENTS

The authors would like to thank Aleksy Kwiatkowski for insightful discussions. AM is partially funded by AITHYRA and the UKRI Engineering and Physical Sciences Research Council (EPSRC) with grant code EP/S024093/1. This research is partially supported by the EPSRC Turing AI World-Leading Research Fellowship No. EP/X040062/1 and EPSRC AI Hub No. EP/Y028872/1.

REFERENCES

Michał Adamaszek and Henry Adams. The vietoris–rips complexes of a circle. *Pacific Journal of Mathematics*, 290(1):1–40, 2017.

Simon Axelrod and Rafael Gomez-Bombarelli. GEOM, energy-annotated molecular conformations for property prediction and molecular generation. *Scientific Data*, 9(1):185, 2022.

John F Beattie, Gloria A Breault, Rebecca PA Ellston, Stephen Green, Philip J Jewsbury, Catherine J Midgley, Russell T Naven, Claire A Minshull, Richard A Pauptit, Julie A Tucker, et al. Cyclin-dependent kinase 4 inhibitors as a treatment for cancer. part 1: identification and optimisation of substituted 4, 6-bis anilino pyrimidines. *Bioorganic & medicinal chemistry letters*, 13(18): 2955–2960, 2003.

Martin Buttenschoen, Garrett M Morris, and Charlotte M Deane. Posebusters: Ai-based docking methods fail to generate physically valid poses or generalise to novel sequences. *Chemical Science*, 15(9):3130–3139, 2024.

Mathieu Carrière, Frédéric Chazal, Yuichi Ike, Théo Lacombe, Martin Royer, and Yuhei Umeda. PersLay: A neural network layer for persistence diagrams and new graph topological signatures. In *International Conference on Artificial Intelligence and Statistics*, pp. 2786–2796. PMLR, 2020.

Mathieu Carrière, Frédéric Chazal, Marc Glisse, Yuichi Ike, Hariprasad Kannan, and Yuhei Umeda. Optimizing persistent homology based functions. In *International conference on machine learning*, pp. 1294–1303. PMLR, 2021.

Jeremy Charlier, Radu State, and Jean Hilger. PHom-GeM: Persistent homology for generative models. In *2019 6th Swiss Conference on Data Science (SDS)*, pp. 87–92. IEEE, 2019.

Andac Demir and Bulent Kiziltan. Multiparameter persistent homology for molecular property prediction. In *ICLR 2023 - Machine Learning for Drug Discovery workshop*, 2023.

Yanyan Diao, Dandan Liu, Huan Ge, Rongrong Zhang, Kexin Jiang, Runhui Bao, Xiaoqian Zhu, Hongjie Bi, Wenjie Liao, Ziqi Chen, et al. Macrocyclization of linear molecules by deep learning to facilitate macrocyclic drug candidates discovery. *Nature Communications*, 14(1):4552, 2023.

Youlong Du, Anas Semghouli, Qian Wang, Haibo Mei, Loránd Kiss, Daniel Baecker, Vadim A Soloshonok, and Jianlin Han. FDA-approved drugs featuring macrocycles or medium-sized rings. *Archiv der Pharmazie*, 358(1):e2400890, 2025.

Herbert Edelsbrunner and John Harer. *Computational topology: an introduction*. American Mathematical Soc., 2010.

Herbert Edelsbrunner, David Letscher, and Afra Zomorodian. Topological persistence and simplification. *Discrete & computational geometry*, 28:511–533, 2002.

Philipp Ermert. Design, properties and recent application of macrocycles in medicinal chemistry. *Chimia*, 71(10):678–678, 2017.

Fabian Falck, Teodora Pandeva, Kiarash Zahirnia, Rachel Lawrence, Richard Turner, Edward Meeds, Javier Zazo, and Sushrut Karmalkar. A fourier space perspective on diffusion models. *arXiv preprint arXiv:2505.11278*, 2025.

Rickard Brüel Gabrielsson, Bradley J. Nelson, Anjan Dwaraknath, and Primoz Skraba. A topology layer for machine learning. In *Proceedings of the Twenty Third International Conference on Artificial Intelligence and Statistics*, volume 108, pp. 1553–1563. PMLR, 2020.

Zhengqi Gao, Kaiwen Zha, Tianyuan Zhang, Zihui Xue, and Duane S Boning. REG: Rectified gradient guidance for conditional diffusion models. In *Forty-second International Conference on Machine Learning*, 2025.

Diego Garcia Jimenez, Vasanthanathan Poongavanam, and Jan Kihlberg. Macrocycles in drug discovery - learning from the past for the future. *Journal of Medicinal Chemistry*, 66(8):5377–5396, 2023.

Fabrizio Giordanetto and Jan Kihlberg. Macrocyclic drugs and clinical candidates: what can medicinal chemists learn from their properties? *Journal of medicinal chemistry*, 57(2):278–295, 2014.

Colin A Grambow, Hayley Weir, Nathaniel L Diamant, Gabriele Scalia, Tommaso Biancalani, and Kangway V Chuang. Accurate and efficient structural ensemble generation of macrocyclic peptides using internal coordinate diffusion. *arXiv preprint arXiv:2305.19800*, 2023.

Yingqing Guo, Hui Yuan, Yukang Yang, Minshuo Chen, and Mengdi Wang. Gradient guidance for diffusion models: An optimization perspective. In *The Thirty-eighth Annual Conference on Neural Information Processing Systems*, 2024.

Saumya Gupta, Dimitris Samaras, and Chao Chen. TopoDiffusionNet: A topology-aware diffusion model. In *International Conference on Learning Representations*, volume 2025, pp. 31699–31713, 2025.

Charles Harris, Kieran Didi, Arian Jamasb, Chaitanya Joshi, Simon Mathis, Pietro Lio, and Tom Blundell. Posecheck: Generative models for 3d structure-based drug design produce unrealistic poses. In *NeurIPS 2023 Generative AI and Biology (GenBio) Workshop*, 2023.

Christian Heinis, Trevor Rutherford, Stephan Freund, and Greg Winter. Phage-encoded combinatorial chemical libraries based on bicyclic peptides. *Nature Chemical Biology*, 5(7):502–507, 2009.

Jonathan Ho, Ajay Jain, and Pieter Abbeel. Denoising diffusion probabilistic models. *Advances in Neural Information Processing Systems*, 33:6840–6851, 2020.

Emiel Hoogeboom, Víctor Garcia Satorras, Clément Vignac, and Max Welling. Equivariant diffusion for molecule generation in 3D. In *Proceedings of the 39th International Conference on Machine Learning*, volume 162, pp. 8867–8887. PMLR, 2022.

Jiangbei Hu, Ben Fei, Baixin Xu, Fei Hou, Weidong Yang, Shengfa Wang, Na Lei, Chen Qian, and Ying He. Topology-aware latent diffusion for 3D shape generation. *arXiv preprint arXiv:2401.17603*, 2024.

Yiming Huang and Tolga Birdal. HOG-Diff: Higher-order guided diffusion for graph generation. *arXiv preprint arXiv:2502.04308*, 2025.

Dapeng Jiang, Xiangzhe Kong, Jiaqi Han, Mingyu Li, Rui Jiao, Wenbing Huang, Stefano Ermon, Jianzhu Ma, and Yang Liu. Zero-shot cyclic peptide design via composable geometric constraints. In *Forty-second International Conference on Machine Learning*, 2025.

Minchuan Jiang, Tianyue Liu, Muzammal Hussain, Yixin Luo, Rui Zheng, Tingjun Hou, Xiaoyun Lu, and Yang Zhou. Macrocycle-DB: a comprehensive database for macrocycle-based drug discovery. *Nucleic Acids Research*, 54(D1):D1469–D1476, 2026.

John Jumper, Richard Evans, Alexander Pritzel, Tim Green, Michael Figurnov, Olaf Ronneberger, Kathryn Tunyasuvunakool, Russ Bates, Augustin Žídek, Anna Potapenko, et al. Highly accurate protein structure prediction with AlphaFold. *nature*, 596(7873):583–589, 2021.

Greg Landrum. RDKit documentation. *Release*, 1(1-79):4, 2013.

Tuan Le, Julian Cremer, Frank Noe, Djork-Arné Clevert, and Kristof T Schütt. Navigating the design space of equivariant diffusion-based generative models for de novo 3d molecule generation. In *The Twelfth International Conference on Learning Representations*, 2024.

Hong Liang, Shengjie Huang, Xinxin Xu, Zhao Yin, Muzammal Hussain, Xiaojuan Song, Jianqiao Yi, Yingqi He, Jing Guo, Zhengchao Tu, et al. Designing macrocyclic kinase inhibitors using macrocycle scaffold hopping with reinforced learning (Macro-Hop). *Journal of Medicinal Chemistry*, 68 (6):6698–6717, 2025.

Christopher A Lipinski, Franco Lombardo, Beryl W Dominy, and Paul J Feeney. Experimental and computational approaches to estimate solubility and permeability in drug discovery and development settings. *Advanced Drug Delivery Reviews*, 23(1-3):3–25, 1997.

Jamie Mallinson and Ian Collins. Macrocycles in new drug discovery. *Future Medicinal Chemistry*, 4(11):1409–1438, 2012.

Matthew R Naylor, Andrew T Bockus, Maria-Jesus Blanco, and R Scott Lokey. Cyclic peptide natural products chart the frontier of oral bioavailability in the pursuit of undruggable targets. *Current Opinion in Chemical Biology*, 38:141–147, 2017.

Joonhyuk Park, Donghyun Lee, Yujee Song, Guorong Wu, and Won Hwa Kim. Topology-aware graph diffusion model with persistent homology. In *The Thirty-ninth Annual Conference on Neural Information Processing Systems*, 2025.

Xingang Peng, Jiaqi Guan, Qiang Liu, and Jianzhu Ma. MolDiff: Addressing the atom-bond inconsistency problem in 3D molecule diffusion generation. In *Proceedings of the 40th International Conference on Machine Learning*, volume 202, pp. 27611–27629. PMLR, 2023.

Adrien Poulenard, Primoz Skraba, and Maks Ovsjanikov. Topological function optimization for continuous shape matching. In *Computer Graphics Forum*, volume 37, pp. 13–25. Wiley Online Library, 2018.

Stephen A Rettie, Katelyn V Campbell, Asim K Bera, Alex Kang, Simon Kozlov, Yensi Flores Bueso, Joshmyn De La Cruz, Maggie Ahlrichs, Suna Cheng, Stacey R Gerben, et al. Cyclic peptide structure prediction and design using AlphaFold2. *Nature Communications*, 16(1):4730, 2025a.

Stephen A Rettie, David Juergens, Victor Adebomi, Yensi Flores Bueso, Qinqin Zhao, Alexandria N Leveille, Andi Liu, Asim K Bera, Joana A Wilms, Alina Üffing, et al. Accurate de novo design of high-affinity protein-binding macrocycles using deep learning. *Nature Chemical Biology*, pp. 1–9, 2025b.

Bastian Rieck. torch_topological: A topological machine learning framework for pytorch, 2022. Commit from December 1, 2022.

Catherine E Rowland, Gustavo Arruda Bezerra, and Michael J Skynner. Rational design of cyclic peptides, with an emphasis on bicyclic peptides. *Current Opinion in Structural Biology*, 92:103025, 2025.

Luca Schaufelberger, Aline Hartgers, and Kjell Jorner. Generating cyclic conformers with flow matching in cremer-pople coordinates. *arXiv preprint arXiv:2601.12859*, 2026.

Yair Schiff, Vijil Chenthamarakshan, Samuel C Hoffman, Karthikeyan Natesan Ramamurthy, and Payel Das. Augmenting molecular deep generative models with topological data analysis representations. In *ICASSP 2022-2022 IEEE International Conference on Acoustics, Speech and Signal Processing (ICASSP)*, pp. 3783–3787. IEEE, 2022.

Arne Schneuing, Charles Harris, Yuanqi Du, Kieran Didi, Arian Jamasb, Ilia Igashov, Weitao Du, Carla Gomes, Tom L Blundell, Pietro Lio, et al. Structure-based drug design with equivariant diffusion models. *Nature Computational Science*, 4(12):899–909, 2024.

Arne Schneuing, Ilia Igashov, Adrian W. Dobbelstein, Thomas Castiglione, Michael M. Bronstein, and Bruno Correia. Multi-domain distribution learning for de novo drug design. In *The Thirteenth International Conference on Learning Representations*, 2025.

Alice T Shaw, Todd M Bauer, Filippo de Marinis, Enriqueta Felip, Yasushi Goto, Geoffrey Liu, Julien Mazieres, Dong-Wan Kim, Tony Mok, Anna Polli, et al. First-line lorlatinib or crizotinib in advanced ALK-positive lung cancer. *New England Journal of Medicine*, 383(21):2018–2029, 2020.

Jascha Sohl-Dickstein, Eric Weiss, Niru Maheswaranathan, and Surya Ganguli. Deep unsupervised learning using nonequilibrium thermodynamics. In *International Conference on Machine Learning*, pp. 2256–2265. PMLR, 2015.

Yang Song and Stefano Ermon. Generative modeling by estimating gradients of the data distribution. *Advances in Neural Information Processing Systems*, 32, 2019.

Yang Song, Jascha Sohl-Dickstein, Diederik P Kingma, Abhishek Kumar, Stefano Ermon, and Ben Poole. Score-based generative modeling through stochastic differential equations. In *International Conference on Learning Representations*, 2021.

Jacob Townsend, Cassie Putman Micucci, John H Hymel, Vasileios Maroulas, and Konstantinos D Vogiatzis. Representation of molecular structures with persistent homology for machine learning applications in chemistry. *Nature communications*, 11(1):3230, 2020.

Lauren A Viarengo-Baker, Lauren E Brown, Anna A Rzepiela, and Adrian Whitty. Defining and navigating macrocycle chemical space. *Chemical science*, 12(12):4309–4328, 2021.

Clement Vignac, Igor Krawczuk, Antoine Siraudin, Bohan Wang, Volkan Cevher, and Pascal Frossard. DiGress: Discrete denoising diffusion for graph generation. In *The Eleventh International Conference on Learning Representations*, 2023a.

Clement Vignac, Nagham Osman, Laura Toni, and Pascal Frossard. MiDi: Mixed graph and 3D denoising diffusion for molecule generation. In *ICLR 2023 - Machine Learning for Drug Discovery workshop*, 2023b.

Liang Wang, Chao Song, Zhiyuan Liu, Yu Rong, Qiang Liu, Shu Wu, and Liang Wang. Diffusion models for molecules: A survey of methods and tasks. *CoRR*, abs/2502.09511, 2025.

Xiaohan Wang and Matthew Berger. Topology guidance: Controlling the outputs of generative models via vector field topology. *arXiv preprint arXiv:2505.06804*, 2025.

Joseph L Watson, David Juergens, Nathaniel R Bennett, Brian L Trippe, Jason Yim, Helen E Eisenach, Woody Ahern, Andrew J Borst, Robert J Ragotte, Lukas F Milles, et al. De novo design of protein structure and function with RFdiffusion. *Nature*, 620(7976):1089–1100, 2023.

Andrei K Yudin. Macrocycles: lessons from the distant past, recent developments, and future directions. *Chemical Science*, 6(1):30–49, 2015.

Xiangxin Zhou, Mingyu Li, Yi Xiao, Jiahan Li, Dongyu Xue, Zaixiang Zheng, Jianzhu Ma, and Quanquan Gu. Designing cyclic peptides via harmonic SDE with atom-bond modeling. In *Forty-second International Conference on Machine Learning*, 2025.

Yael Ziv, Fergus Imrie, Brian Marsden, and Charlotte M Deane. MolSnapper: conditioning diffusion for structure-based drug design. *Journal of Chemical Information and Modeling*, 65(9):4263–4273, 2025.

A Additional Related Literature

A.1 Cyclic Peptide Generation

Most existing approaches focus on a restricted subclass of macrocycles, called cyclic peptides, where all building blocks are amino acids linked by peptide bonds. AfCycDesign adapts the AlphaFold framework (Jumper et al., 2021) by encoding cyclicity through a modified positional encoding, enabling the generation and structural prediction of cyclic peptides (Rettie et al., 2025a). Similarly, RFpeptides builds on RFdiffusion (Watson et al., 2023) and introduces a cyclic relative positional encoding to generate macrocyclic peptide backbones (Rettie et al., 2025b). Other works instead incorporate explicit geometric constraints or harmonic SDE formulations Jiang et al. (2025); Zhou et al. (2025). However, the design space of cyclic peptides is substantially smaller and more structured than that of general macrocycles, making the generation task comparatively easier. As a result, these methods do not readily extend to the broader and more diverse class of non-peptidic macrocycles.

Additionally, a closely related problem is the prediction of 3D macrocyclic conformations from a given 2D molecular graph. This task was addressed by RINGER, which introduced a diffusion-based transformer model to generate ensembles of 3D conformations for macrocyclic peptides (Grambow et al., 2023). More recently, PuckerFlow proposed a flow-matching approach operating in Cremer-Pople space to generate conformers of small cyclic molecules Schaufelberger et al. (2026).

A.2 Applications of Persistent Homology in Machine Learning

General use of persistent homology in ML. Persistent homology (PH) has established itself as a critical framework in machine learning for characterizing data topology across multiple scales. Early integration strategies focused on creating differentiable, topology-aware architectures and losses. Notably, Topology Layer (Gabrielsson et al., 2020) and PersLay (Carrière et al., 2020) allow deep neural networks to directly process persistence diagram features. PHom-GeM (Charlier et al., 2019) instead introduced a topological loss function based on the bottleneck distance, ensuring that generated distributions faithfully reproduce the topology of the training set.

Applications to diffusion models. More recently, topological insights have been effectively adapted for diffusion-based generative frameworks across image, 3D, and graph domains. In the context of 3D and visual generation, Topology-Aware Latent Diffusion models (Hu et al., 2024) leverage PH to guide the formation of 3D shapes with specific topological characteristics. Similarly, Wang & Berger (2025) demonstrated that diffusion models can be steered using coordinate-based networks to satisfy rigorous topological constraints, while TopoDiffusionNet (Gupta et al., 2025) introduced a differentiable mechanism to regulate the number of objects (0-dim) and holes (1-dim) in generated image masks. In the graph domain, PH is increasingly used to capture complex connectivity; Park et al. (2025) developed a loss function based on persistence diagram matching for graph diffusion, and HOG-Diff (Huang & Birdal, 2025) introduced a framework for generating higher-order structures via cell complex filtering and spectral diffusion.

Molecular applications. In the realm of chemistry, persistent homology has proven effective for encoding molecular structure into ML-friendly representations. Townsend et al. (2020) introduced persistence images, 2D embeddings of PH-derived features, as molecular fingerprints to screen vast chemical libraries like GDB-9. Later, Demir & Kiziltan (2023) extended this with multiparameter PH fingerprints, incorporating atomic descriptors such as partial charges and bond types to enhance property prediction tasks. Finally, TDA has been used to augment a VAE with topological molecule representations which resulted in an improvement over a range of molecular generation metrics (Schiff et al., 2022).

B Discussion and Future Work

Leveraging base model advancements. Since MacroGuide enhances generation metrics, it is well-positioned to benefit from rapid advancements in base model architectures. A promising avenue for future work is the integration of MacroGuide with recent, high-capacity models, potentially unlocking even greater performance.

Bond-level information. Our method relies on atomic positions to enforce macrocyclicity, without explicitly constraining the neighboring atoms in the cycle to form bonds. This design naturally aligns with point-cloud-based models such as EDM, which do not represent bonds explicitly (Hoogeboom et al., 2022). For architectures that additionally model bond information (e.g., MolDiff), one could in principle incorporate bond-level constraints into the guidance. Our preliminary investigations (Appendix K) suggest that the added complexity of this approach outweighs the potential benefits, though it remains an open option for future work.

Explicit hydrogens. We apply MacroGuide to models that do not explicitly model hydrogens during training, a common setting in recent works, as the hydrogens can be easily inferred during post-processing to avoid unnecessary time and memory overhead. However, if one chooses to work with a model that represents hydrogens explicitly, their monovalence can hinder cycle closure. In this case, a simple workaround is to exclude hydrogens from the Vietoris-Rips complex.

Synthetic accessibility. Macrocycles offer attractive pharmacological properties, but their synthesis typically involves an additional entropic cost associated with ring closure. As macrocycle-generating models move closer to practical deployment, incorporating synthetic considerations will become increasingly important. A natural and promising next step is to integrate synthesis-aware constraints and retrosynthetic planning into the generative process, enabling closer alignment between generated candidates and experimentally accessible chemistries.

C Macrocycle Size Control

Combinatorial and geometric sizes. The *size* of a macrocycle is defined here as the number n of heavy atoms it contains. However, we only have direct control over a geometric notion of size, which is the *death* of the corresponding H_1 component in the Vietoris-Rips filtration. Therefore we need to establish an explicit relationship between these two definitions.

A convenient and analytically tractable way to do so is to consider an idealized but informative model: an equilateral polygon with n vertices embedded in the plane (representing atoms), and edges of length ℓ (representing bonds). However, regularity is not a realistic assumption as tetrahedral carbon arrangements impose smaller bond angles than the ones of a regular polygon ($\theta = 109.5°$, which can be observed in Figure 2). We thus study crown-shaped equilateral n-gons with interior angles θ (see Figure 8 of Appendix D for a visualization). The following theorem provides a simple relationship $n = f(d, \ell)$ in this framework.

Theorem C.1 (Vietoris-Rips death time of a tetrahedral cycle)**.** *Consider a regular cyclic conformation of n atoms (n even) with bond length ℓ and bond angle θ. The death time d of the dominant H_1 component in the Vietoris-Rips filtration is given by:*

$$d = \ell\sqrt{2(1-\cos\theta)} \cdot \frac{\sin\left(\lceil \frac{n}{6} \rceil \frac{2\pi}{n}\right)}{\sin\left(\frac{2\pi}{n}\right)} \tag{7}$$

In the limit of large n,

$$n = \frac{4\pi}{\sqrt{6(1-\cos\theta)}} \frac{d}{\ell} + \mathcal{O}(1) \tag{8}$$

Accuracy of the linear approximation. Solving Equation equation 7 for n does not admit an easy closed-form solution, making the linear approximation of Equation 8 very attractive from a practical point of view, assuming it is tight enough. Consider a macrocycle of size $n = 14$ (crown shaped) with a typical bond length $\ell = 1.5$ Å, and $\theta = 109.5°$. The linearization provided incurs a relative error of approximately 3%. This confirms that for drug-like macrocycles, the higher-order terms are negligible in practice. We further validate Equation 8 empirically in Section 4.3.1.

Lemma C.2 (Vietoris-Rips death time of a regular n-gon)**.** *Consider a regular n-gon of side length ℓ. The death time d of the dominant H_1 component in the Vietoris-Rips filtration is given by:*

$$d = \ell \frac{\sin\left(\lceil \frac{n}{3} \rceil \frac{\pi}{n}\right)}{\sin\left(\frac{\pi}{n}\right)}$$

Proof of Lemma C.2. Following the theory of Vietoris-Rips complexes of the circle established by Adamaszek & Adams (2017), the homotopy type of $VR(X; r)$ for a finite subset $X \subset S^1$ is determined by its winding fraction $wf(X; r)$. For a regular n-gon with side length ℓ, the complex is equivalent to the clique complex of the cyclic graph C_n^k.

Threshold for death: The H_1 component persists as long as the winding fraction satisfies $0 < wf < 1/3$.

Geometric jump: For a regular n-gon, the winding fraction is defined as $wf = k/n$, where k is the maximum number of edges a single chord of length d can span. Thus, death occurs at the smallest d such that $k = \lceil n/3 \rceil$.

Exact formula: Let R be the circumradius of the n-gon. The side length ℓ and the death distance d are chords related by:

$$\ell = 2R \sin\left(\frac{\pi}{n}\right), \quad d = 2R \sin\left(\lceil n/3 \rceil \frac{\pi}{n}\right)$$

Dividing these yields the exact relation:

$$d = \ell \frac{\sin\left(\lceil \frac{n}{3} \rceil \frac{\pi}{n}\right)}{\sin\left(\frac{\pi}{n}\right)}$$

□

Proof of Theorem C.1. **Extension to tetrahedral conformation:** Consider n atoms in a zigzag cycle. Because the bond angles are constrained, the atoms alternate between two concentric radii. Death edges can only be between two of the $n/2$ atoms of the interior circle. These atoms form a planar regular N-gon where $N = n/2$. That means we can apply Lemma C.2. The proof geometry is illustrated in Figure 8.

Effective side length: The distance between two adjacent atoms in this sub-polygon is determined by the bond length ℓ and the bond angle θ. More precisely the law of cosines gives

$$\ell' = \sqrt{\ell^2 + \ell^2 - 2\ell^2 \cos\theta} = \ell\sqrt{2(1 - \cos\theta)}$$

Exact formula: Substituting $N = n/2$ and ℓ' into the Lemma:

$$d = \ell\sqrt{2(1 - \cos\theta)} \cdot \frac{\sin\left(\lceil \frac{n}{6} \rceil \frac{2\pi}{n}\right)}{\sin\left(\frac{2\pi}{n}\right)}$$

Linearization: As $n \to +\infty$, we get

$$d \approx \ell\sqrt{2(1 - \cos\theta)} \frac{\sqrt{3}/2}{2\pi/n} = \frac{n\ell\sqrt{6(1 - \cos\theta)}}{4\pi}$$

Solving for n yields the linear form:

$$n = \frac{4\pi}{\sqrt{6(1 - \cos\theta)}} \frac{d}{\ell} + \mathcal{O}(1)$$

□

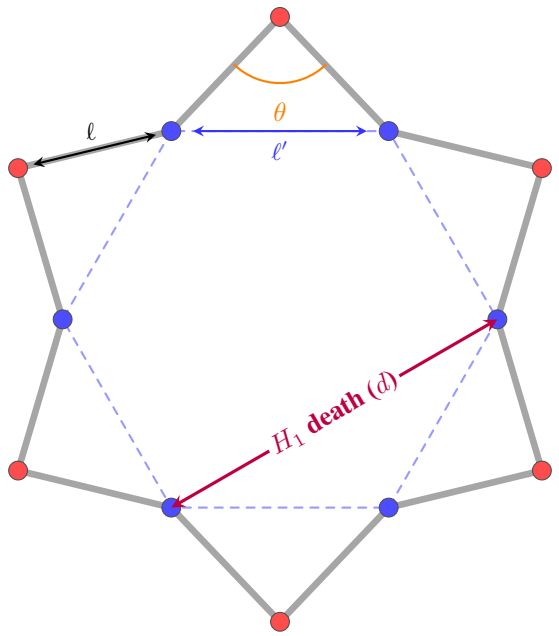

Figure 8: **Proof geometry: crown-shaped n-gon ($n = 12$).** The inner polygon (dashed blue) determines the filtration death time d. The effective side length ℓ' is derived from the bond length ℓ and the interior bond angle.

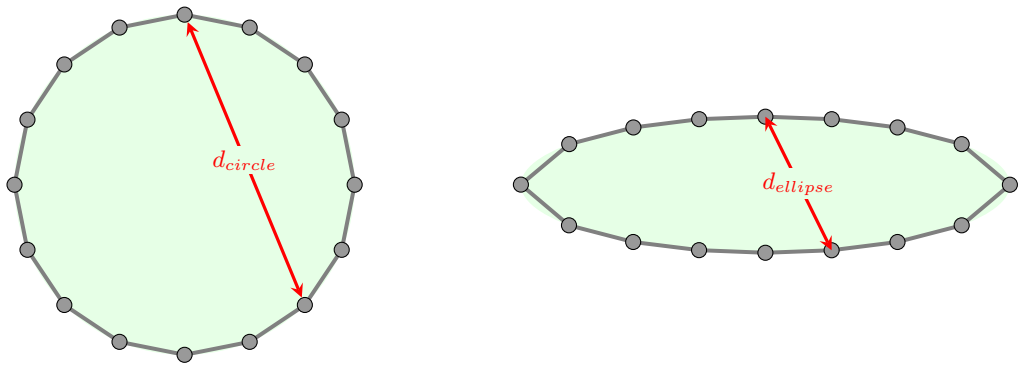

(a) Circular Ring

(b) Elliptical Ring

Figure 9: **Impact of cycle shape on H_1 death ($n = 16$).** In an elongated elliptical macrocycle, the death time $d_{ellipse}$ is significantly reduced compared to d_{circle}. The death times were obtained numerically using `torch_topological`.

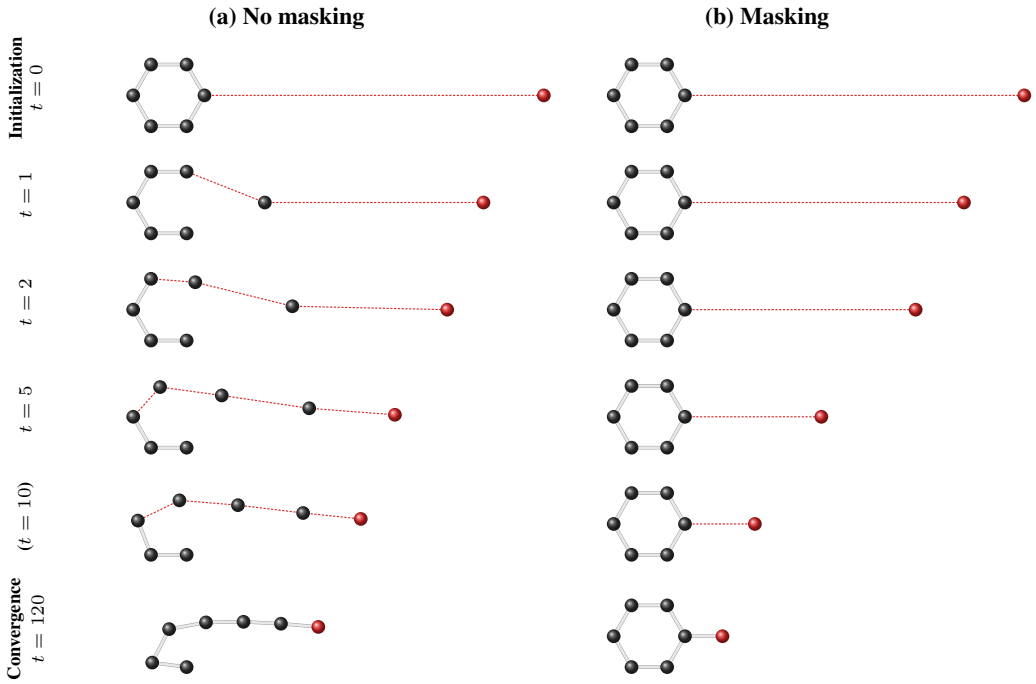

Figure 10: **Failure mode analysis.** Comparison of optimization dynamics under Equation (9). (a) Symmetric gradients cause "unzipping." (b) Masked gradients preserve structure.

D Details on $F^{H_0}_{\text{death}}$: Gradient Masking for Stability

Method. As presented in Section 3.1, connectivity is enforced by minimizing the H_0 persistence death times that exceed a threshold $\ell^\star$. In the Vietoris-Rips filtration, a finite H_0 death time corresponds to the scale at which two connected components merge. Formally, the connectivity loss is defined over the set of finite death times $\mathcal{D}_0(X)$ in the 0-dimensional persistence diagram:

$$F^{H_0}_{\text{death}}(X) = \sum_{d \in \mathcal{D}_0(X)} \Big(\text{ReLU}\big(d - \ell^\star\big)\Big)^2 \tag{9}$$

To optimize this objective, we introduce a **masked gradient** scheme. Each death value $d > \ell^\star$ is determined by the distance between two specific atoms (u, v) that trigger the merging of two components (i.e., $\|x_u - x_v\| = d$). We define the centroid of the system as $\mathbf{c} = \frac{1}{N}\sum_{i=1}^{N} x_i$. The gradient applied to each endpoint of this critical edge goes through by a binary mask m:

$$g_u = m_u \cdot \nabla_{x_u} F^{H_0}_{\text{death}}, \quad m_u = \mathbb{1}\left(\|x_u - \mathbf{c}\| \geq \|x_v - \mathbf{c}\|\right)$$

In other words, for every pair of atoms responsible for the merging of two connected components (that are separated by more than $\ell^\star$), we block the gradient flow for the atom closer to the centroid ($m = 0$) and allow it only for the atom further away ($m = 1$).

Instability of symmetric optimization. The necessity of this masking becomes apparent when analyzing the case of a stable connected cluster $\mathcal{C}$ (stable in the sense that all the H_0 death times are less than $\ell^\star$) interacting with a distant outlier component o. Let's assume that the merging of the outlier with the cluster determines a death time $d = \|x_u - x_o\| > \ell^\star$, for some $u \in \mathcal{C}$ (i.e. the outlier is at a distance d from the cluster). Without masking, the gradient of Equation (9) is applied symmetrically. The internal atom u moves as

$$\Delta x_u \propto -\nabla_{x_u} F^{H_0}_{\text{death}} \propto (x_o - x_u)$$

Since o is an outlier, this vector points away from the cluster centroid. Consequently, u is pulled out of its local equilibrium within $\mathcal{C}$. This displacement stretches the distances between u and its neighbors.

If the force exerted by the outlier is sufficiently strong (i.e., if it is sufficiently far), these internal distances cross the threshold $\ell^\star$, creating new high-persistence H_0 features that trigger their own penalty terms in Eq. 9. This creates a cascading failure where the cluster is sequentially pulled apart, resulting in the *linearization* or "unzipping" of the cycle structure, as demonstrated in Figure 10a. By clamping the inner atom u (via $m_u = 0$), our method decouples the outlier's transport from the cluster's internal dynamics, ensuring structural preservation (Figure 10b).

Non-conservative field. Note that this masking renders the resulting guidance vector field non-conservative, effectively acting as a stabilized approximation of the exact score function described in Equation (6). Nevertheless, the theoretical intuition provided in Section 3.2 remains relevant, as the masked update still locally maximizes the conditional likelihood $p_t(y|x)$ to drive the system toward the desired topology, differing only by the suppression of specific unstable gradient directions.

E Topological Features and Their Gradients Throughout Denoising

To better understand the success of MacroGuide, we analyze the evolution of the topological features and their associated gradients throughout the 1000 steps of the reverse diffusion process.

Feature convergence and constraint satisfaction. As shown in Figure 11, the guidance successfully steers the molecule toward the target topology. All optimized features converge rapidly to their respective targets: the largest cycle size (H_1 death) reaches the target interval within the first few hundred steps, while cycle connectivity (H_1 birth) and molecular connectivity (H_0 death) are effectively kept below the threshold $\ell^\star$. Once satisfied, these constraints remain stable throughout the remainder of the denoising process, ensuring that the global macrocyclic structure is established early and preserved.

Gradient analysis. Figure 14 illustrates that, on average, the topological gradients are of the same magnitude as the denoising gradients. We observe that H_1 death gradients are dominant at the very beginning of the process, driving the initial ring expansion. The H_1 birth gradients, while sparse throughout the trajectory, are constant in norm by design, providing sharp corrections when edges exceed the threshold $\ell^\star$. Crucially, in the last 100 steps (where fine-grained chemical details such as bond orders and angles are finalized) the gradients are dominated almost exclusively by the denoising term. This explains the success of our method: the guidance effectively pushes the molecule into a stable macrocyclic state early on, allowing the denoiser to perform optimal local validity optimization in the final stages without interference.

Comparison with squared H_1 birth. We compare this behavior with the one achieved by squaring the formula of $F^{H_1}_{\text{birth}}$ as is done for the other guidance terms. As seen in Figure 13, the H_1 birth feature in the squared setting stays very close to the target $\ell^\star$ but tends to oscillate around it rather than remaining strictly below. This behavior is confirmed by the gradient analysis in Figure 15, which shows that H_1 birth gradients remain very significant and exceeds the denoising gradients, even during the last 100 steps. Following the reasoning above, this persistent perturbation interferes with the denoiser's validity optimization in the critical final phase, explaining the lower performance observed with the squared H_1 birth term.

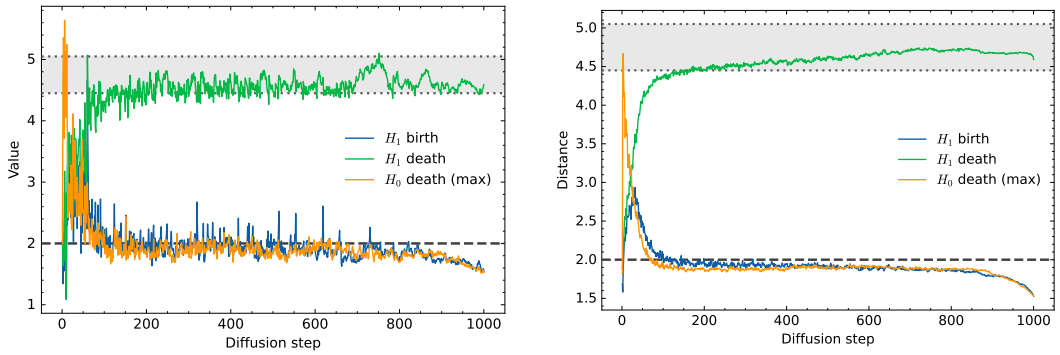

Figure 11: Topological features (no square on $F^{H_1}_{\text{birth}}$) for individual runs (left) and averaged runs (right).

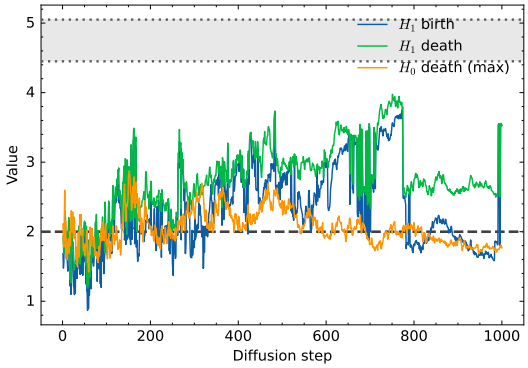

Figure 12: Topological features without guidance

F Detailed Algorithms

We present the detailed algorithms used by MacroGuide. Algorithm 1 shows how MacroGuide fits into the overall scheme of denoising. Algorithm 2 describes the high-level structure of MacroGuide, whereas algorithms 3 and 4 describe its components: H_1 and H_0 guidances, respectively.

Relationship to continuous score matching. We note a specific detail regarding the implementation of topological guidance in Algorithm 1 compared to the theoretical formulation in Equation (1). While Equation (1) defines guidance as a modification to the instantaneous score function $\nabla_{x_t} \log p_t(y|x_t)$,

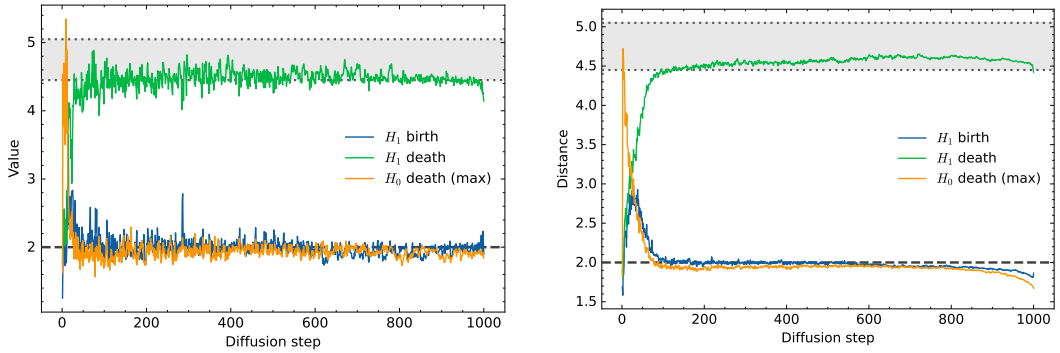

Figure 13: Topological features **with squared** $F^{H_1}_{\text{birth}}$ for individual runs (left) and averaged runs (right).

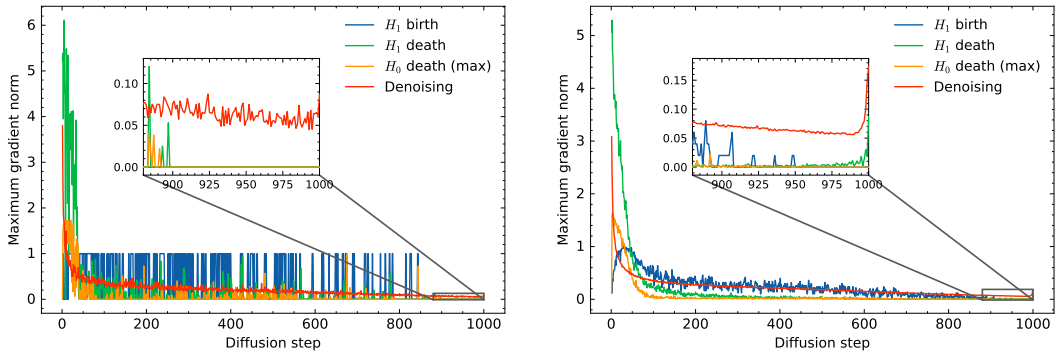

Figure 14: Gradient statistics (no square on $F^{H_1}_{\text{birth}}$) for individual runs (left) and averaged runs (right).

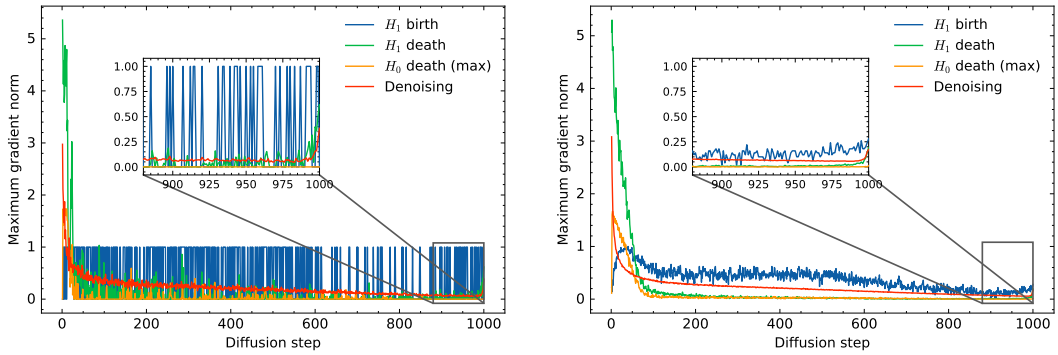

Figure 15: Gradient statistics **with squared** $F^{H_1}_{\text{birth}}$ for individual runs (left) and averaged runs (right).

our algorithm implements this as a sequential predictor-corrector step. Specifically, we first apply the base denoising update to obtain an intermediate state x_{t-1}, and then calculate the topological gradient Δ on this cleaner state. In this discrete setting, the scalar weight λ acts as an effective step size that implicitly absorbs the SDE integration constants (e.g., σ_t^2) required to map the score-space gradient to a coordinate-space displacement.

Algorithm 1 DENOISEWITHMACROGUIDE

Input: denoiser ϵ_θ; noise schedule $\{\sigma_t\}_{t=1}^T$; initial sample $\mathbf{x}_T$; guidance parameters $(\lambda, \ell^*, d_{\min}, d_{\max})$, guidance schedule $\mathcal{T}_g \subset \{1, \ldots, T\}$
for $t = T$ **down to** 1 **do**
  $\hat{\epsilon} \leftarrow \epsilon_\theta(\mathbf{x}_t, \sigma_t)$
  $\mathbf{x}_{t-1} \leftarrow$ DENOISEUPDATE$(\mathbf{x}_t, \hat{\epsilon}, \sigma_t)$
  if $t \in \mathcal{T}_g$ **then**
    $\Delta \leftarrow$ MACROGUIDE$(\mathbf{x}_{t-1}; \ell^*, d_{\min}, d_{\max})$ {Algorithm 2}
    $\mathbf{x}_{t-1} \leftarrow \mathbf{x}_{t-1} + \lambda \cdot \Delta$
  end if
end for
return $\mathbf{x}_0$

Algorithm 2 MACROGUIDE

Input: Coordinates $\mathbf{X}$, $\ell^*, d_{\min}, d_{\max}$
$\Pi \leftarrow$ VietorisRips($\mathbf{X}$)
$\mathbf{g}_{H_1} \leftarrow H_1$GUIDANCE($\mathbf{X}, \Pi, \ell^*, d_{\min}, d_{\max}$) {Algorithm 3}
$\mathbf{g}_{H_0} \leftarrow H_0$GUIDANCE($\mathbf{X}, \Pi, \ell^*$) {Algorithm 4}
$\Delta \leftarrow -(\mathbf{g}_{H_1} + \mathbf{g}_{H_0})$
Return Δ

Algorithm 3 H_1GUIDANCE

Input: coordinates X, persistence info Π, thresholds $\ell^\star, d_{\min}, d_{\max}$
Initialize objectives $F^{H_1}_{\text{birth}} \leftarrow 0, \quad F^{H_1}_{\text{death}} \leftarrow 0$
for each sample k in batch **do**
  Extract H_1 diagram pairs P from Π_k
  if P is empty **then**
    continue
  end if
  {Identify the H_1 component (ring) that dies last}
  Find index $i^\star = \arg\max_i \text{death}(P_i)$
  Retrieve critical vertices for feature $i^\star$:
    (u_b, v_b) defining birth time $b^{(1)}_{i^\star}$
    (u_d, v_d) defining death time $d^{(1)}_{i^\star}$
  1. Cycle Connectivity (H_1 birth):
  $b^{(1)}_{i^\star} \leftarrow \|x_{u_b} - x_{v_b}\|$
  $F^{H_1}_{\text{birth}} \leftarrow F^{H_1}_{\text{birth}} + \text{ReLU}(b^{(1)}_{i^\star} - \ell^\star)$
  2. Cycle Size (H_1 death):
  $d^{(1)}_{i^\star} \leftarrow \|x_{u_d} - x_{v_d}\|$
  {Penalize if outside target interval $[d_{\min}, d_{\max}]$}
  if $d^{(1)}_{i^\star} < d_{\min}$ **then**
    $F^{H_1}_{\text{death}} \leftarrow F^{H_1}_{\text{death}} + (d_{\min} - d^{(1)}_{i^\star})^2$
  else if $d^{(1)}_{i^\star} > d_{\max}$ **then**
    $F^{H_1}_{\text{death}} \leftarrow F^{H_1}_{\text{death}} + (d^{(1)}_{i^\star} - d_{\max})^2$
  end if
end for
$\mathcal{F}^{(1)}_{\text{TDA}} \leftarrow F^{H_1}_{\text{birth}} + F^{H_1}_{\text{death}}$
Compute gradients $\mathbf{g}_{H_1} \leftarrow \nabla_X \mathcal{F}^{(1)}_{\text{TDA}}$
Return $\mathbf{g}_{H_1}$

Algorithm 4 H_0GUIDANCE

Input: coordinates X, persistence info Π, threshold $\ell^\star$
Initialize connectivity objective $F_{\text{death}}^{H_0} \leftarrow 0$
for each sample pair $(X^{(k)}, \pi)$ in (X, Π) **do**
  Extract finite death times $\mathcal{D}_0(X^{(k)})$ and corresponding pairs P from π
  Identify active edges $E \leftarrow \{(u, v) \in P \mid \text{death}(u, v) > \ell^\star\}$
  if E is empty **then**
    continue
  end if
  $\mathbf{c} \leftarrow \frac{1}{N} \sum_j x_j$ {Calculate centroid of molecule k}
  for each critical edge (u, v) in E **do**
    {Apply masked gradient: move only the atom furthest from centroid}
    if $\|x_u - \mathbf{c}\| > \|x_v - \mathbf{c}\|$ **then**
      u is active $(m_u = 1)$, v is masked $(m_v = 0)$
      $x_{active} \leftarrow x_u, \quad x_{masked} \leftarrow \text{stop_gradient}(x_v)$
    else
      v is active $(m_v = 1)$, u is masked $(m_u = 0)$
      $x_{active} \leftarrow x_v, \quad x_{masked} \leftarrow \text{stop_gradient}(x_u)$
    end if
    $d_j^{(0)} \leftarrow \|x_{active} - x_{masked}\|$
    $F_{\text{death}}^{H_0} \leftarrow F_{\text{death}}^{H_0} + \left(\text{ReLU}(d_j^{(0)} - \ell^\star)\right)^2$
  end for
end for
$\mathbf{g}_{H_0} \leftarrow \nabla_X F_{\text{death}}^{H_0}$
Return $\mathbf{g}_{H_0}$

G EXPERIMENTAL DETAILS

G.1 MOLDIFF TRAINING DATASET

The training split used for MolDiff contains 231,521 data points from GEOM-Drugs, out of which only 323 molecules had a ring of at least 12 atoms Axelrod & Gomez-Bombarelli (2022); Peng et al. (2023).

G.2 PROTEIN CONDITIONING WITH MOLSNAPPER

Following the original setup, we selected a subset of atoms from the reference ligand to define a pharmacophore and used the provided protein pocket corresponding to PDB ID 1H00 Ziv et al. (2025); Beattie et al. (2003). We included all nitrogen atoms from the reference ligand, as these are the most likely to participate in specific interactions with the protein pocket and thus provide a strong conditioning signal. In total, the pharmacophore consists of five atoms: three nitrogens and two carbons.

G.3 COMPUTATIONAL RESOURCES

All experiments were conducted on NVIDIA A10 GPUs, except for finetuning which was performed on NVIDIA H100 GPUs.

H ADDITIONAL BASELINES

This section provides descriptions of the baselines used to benchmark MACROGUIDE in Tables 1 and 2.

H.1 FINETUNING

We finetune MolDiff using the publicly released pretrained checkpoint and continue training on a macrocycle-specific dataset Peng et al. (2023). The finetuning procedure follows the original training protocol, and was run for 50,000 iterations. Due to the increased size of macrocyclic molecules relative to those in the original training set, which leads to higher memory consumption during training, we reduce the batch size from 256 to 64 to fit within hardware constraints.

The macrocyclic dataset is derived from Macrocycle-DB Jiang et al. (2026), which contains 45,525 macrocyclic compounds with resolved three-dimensional structures. We follow the data processing pipeline of MolDiff Peng et al. (2023) and apply the same filtering criteria, in particular removing molecules containing atom types not present in the pretrained model. After filtering, 40,496 molecules remain. We split the resulting dataset into training and validation sets using an 85:15 ratio, yielding 34,422 training molecules and 6,074 validation molecules, which are used to monitor and control the finetuning process.

Because MolSnapper uses similar underlying architecture and checkpoints as MolDiff, it is possible to use the same finetuned denoising network in both models.

H.2 NAIVE TOPOLOGICAL GUIDANCE

Naive geometric cycle guidance. We introduce a simple geometric guidance term that biases generated molecular point clouds toward forming a single macrocyclic structure. Importantly, we do *not* assume that the atoms are ordered along a ring. Instead, given a molecule with at least n atoms, we select an arbitrary subset of n atoms (e.g., the first n atoms in the representation) and impose a virtual cyclic ordering solely for the purpose of defining the guidance objective. This ordering has no chemical meaning and is used only to provide a differentiable proxy for cyclic topology.

Let

$$X = (x_0, \ldots, x_{n-1}) \in \mathbb{R}^{n\times 3}$$

denote the coordinates of the selected atoms. We define two complementary geometric constraints: a local adjacency constraint encouraging ring closure, and a global separation constraint preventing degenerate, collapsed configurations.

Local cyclic adjacency. We enforce approximate uniformity of distances between consecutive atoms in the imposed cyclic order. Defining

$$\ell_i = \|x_i - x_{i+1}\|_2, \qquad x_n \equiv x_0,$$

we penalize distances that fall outside a target interval $[\ell_{\min}, \ell_{\max}]$. This is implemented using a hinge-squared penalty:

$$\mathcal{L}_{\text{edge}}(X) = \sum_{i=0}^{n-1} \Big[\max(0, \ell_{\min} - \ell_i)^2 + \max(0, \ell_i - \ell_{\max})^2\Big].$$

In our experiments, we set $\ell_{\min} = 1.0$ Å and $\ell_{\max} = 2.0$ Å. This term encourages the selected atoms to form a closed loop with approximately consistent edge lengths, without requiring exact bond formation or atom ordering.

Global anti-collapse constraint. To avoid degenerate solutions in which the loop collapses or folds onto itself, we introduce a coarse global constraint based on opposite atoms in the imposed cycle. For even n, we define

$$o_i = \|x_i - x_{i+n/2}\|_2,$$

and penalize opposite pairs that are closer than a minimum separation $o_{\min}$:

$$\mathcal{L}_{\text{opp}}(X) = \sum_{i=0}^{n-1} \max(0, o_{\min} - o_i)^2.$$

We set $o_{\min} = 3.0$ Å in all experiments. This term encourages a non-degenerate ring geometry with a finite diameter, discouraging self-intersections and collapsed configurations.

Overall guidance objective. The guidance is then given by the sum of $\mathcal{L}_{\text{edge}}$ and $\mathcal{L}_{\text{opp}}$. While this objective does not explicitly compute topological invariants such as persistent homology, it provides a computationally inexpensive and fully differentiable surrogate that promotes cycle-like geometries. In particular, it biases generation toward configurations exhibiting both local loop closure and global ring structure, despite the absence of any predefined atom ordering or explicit topological constraints.

H.3 Solid-torus Noise Initialization

We replace standard Gaussian initialization with a prior distribution supported on a solid torus, defined by major radius $R = 2.5$ Å and tube radius $r_{\text{max}} = 1.5$ Å. The coordinates $\mathbf{x} \in \mathbb{R}^3$ are sampled according to:

$$\begin{aligned} x &= (R + \rho\cos\phi)\cos\theta, \\ y &= (R + \rho\cos\phi)\sin\theta, \\ z &= \rho\sin\phi, \end{aligned}$$

where $\theta, \phi \sim \mathcal{U}[0, 2\pi)$ are uniform angular coordinates. The radial offset ρ determines the deviation from the torus core and is sampled as $\rho = r_{\text{max}} \cdot \xi$, where $\xi \sim \text{Beta}(0.5, 2.0)$. This choice of hyperparameters ($\alpha < 1$) concentrates the probability mass near the central filament ($\rho \to 0$) while maintaining support throughout the tube.

Prior mismatch. Note that this initialization strategy fundamentally violates the stationary assumptions of the standard diffusion reverse process Song et al. (2021), which is trained to map from an isotropic Gaussian prior. The negative results of Tables 1 and 2 are therefore not surprising.

I Additional Visualizations

I.1 Unconditional Generation

Figure 16 displays molecules generated by MolDiff+MacroGuide, for the parameter values described in Section 4.1.1.

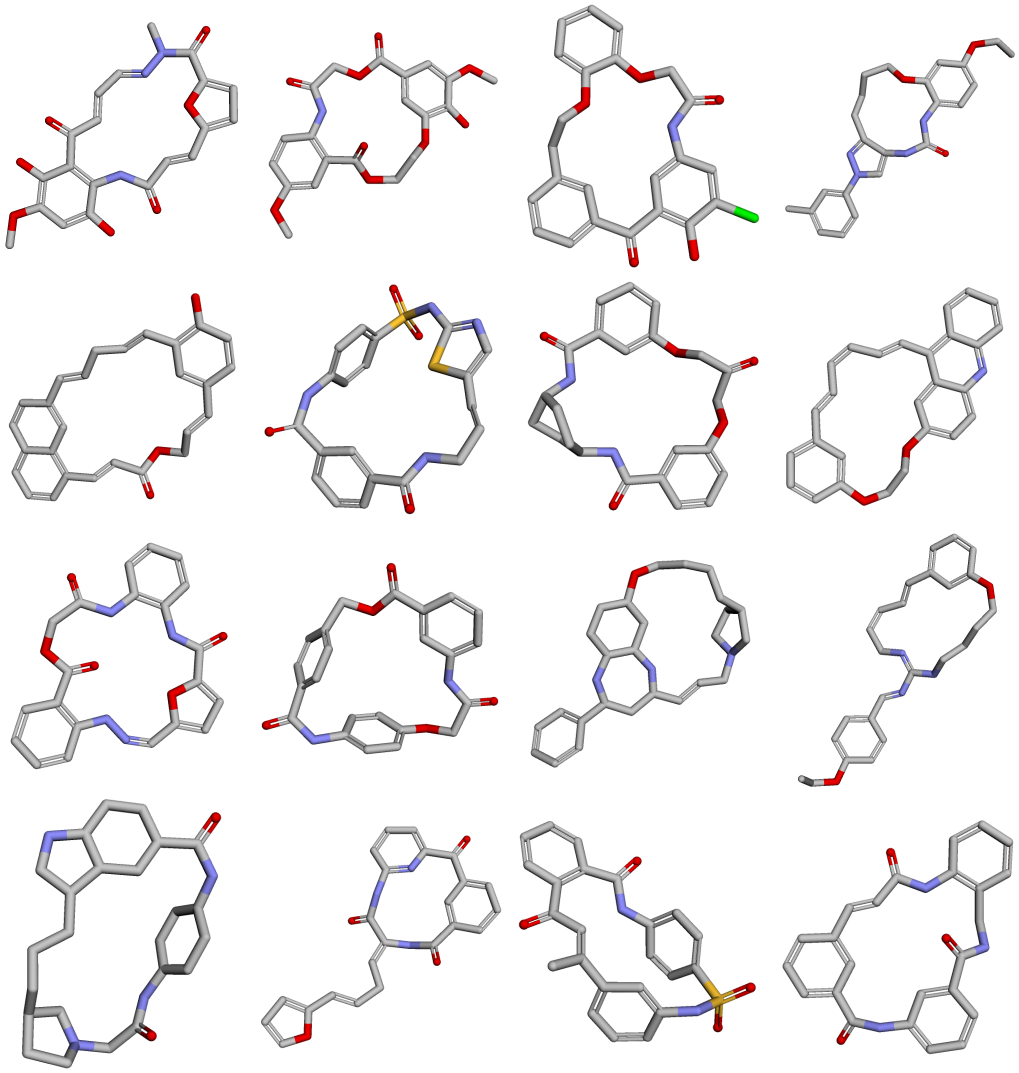

Figure 16: **Visualizations of generated molecules in the unconditional setting.**

I.2 CONDITIONAL GENERATION

Figure 17 displays molecules generated by MolSnapper+MACROGUIDE, for the parameter values described in Section 4.1.2.

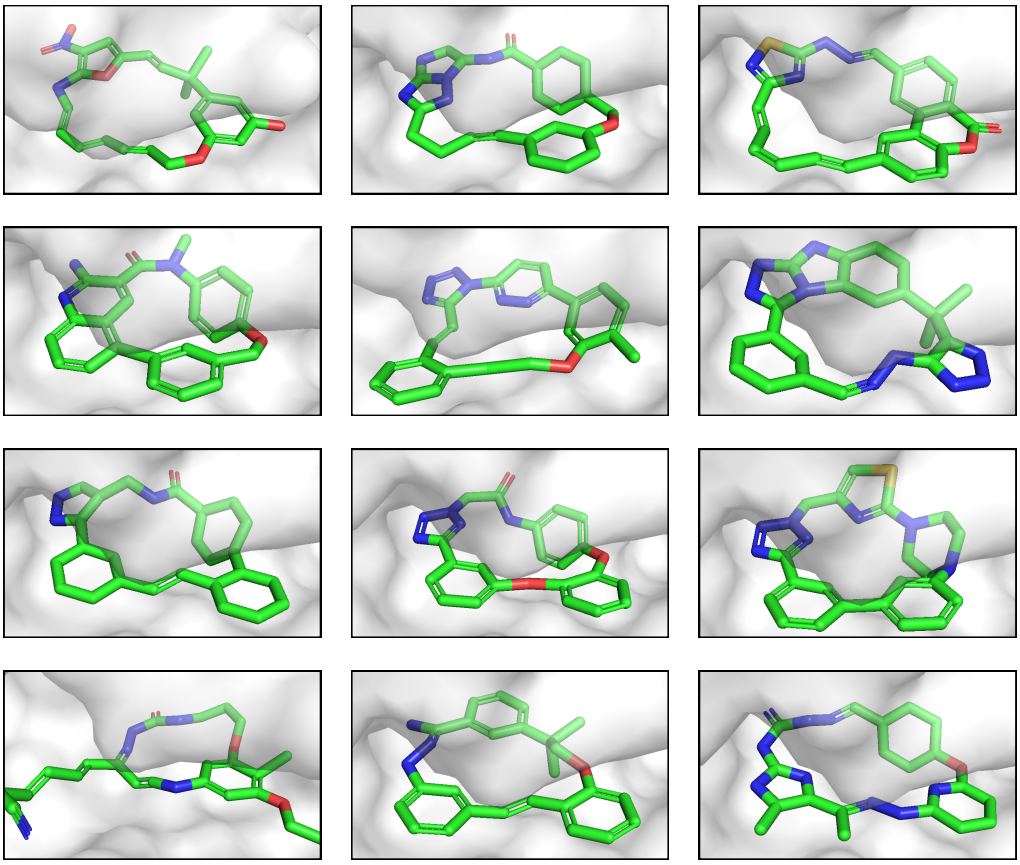

Figure 17: **Visualizations of generated molecules in the protein-conditioned setting.** The top parts of molecules are less visible because they are obstructed by a semi-transparent protein pocket.

J ADDITIONAL RESULTS

J.1 STANDARD DEVIATIONS

In Table 5 we report standard deviations for our experiments. The metric results were computed on 5 sets of 1000 molecules.

Table 5: **Standard deviations of unconditional and protein-conditioned macrocycle generation performance.** The last 6 values do not appear for MolDiff as the metrics are defined only in the protein-conditioning setting. Variances for unguided MolDiff and MolSnapper are not reported as generating multiple sets of 1000 macrocycles proved computationally prohibitive due to the very low baseline macrocycle success rates.

Metrics (↑; [0-1])	MolDiff +MACROGUIDE	MolSnapper +MACROGUIDE
Validity	±.003	±.008
Connectivity	±.001	±.000
Successfulness	±.003	±.008
Out of successful:		
Macrocycles	±.002	±.003
Out of macrocycles:		
Diversity	±.005	±.001
Novelty	±.000	±.001
Uniqueness	±.001	±.001
All PoseBusters tests	-	±.015
Ligand PoseBusters	±.013	±.018
Bond lengths	±.004	±.010
Bond angles	±.002	±.012
Internal steric clash	±.013	±.017
Aromatic ring flatness	±.001	±.002
Non-ar. ring non-flatness	±.001	±.001
Double bond flatness	±.004	±.002
Internal energy	±.004	±.010
Protein PoseBusters	-	±.008
Protein-ligand max. distance	-	±.000
Min. distance to protein	-	±.008
Volume overlap with protein	-	±.000
Pharmacophore satisfaction	-	±.014
Macrocycle Lipinski	-	±.017

J.2 ABLATIONS OF GUIDANCE TERMS

We perform ablations to show the influence of H_1 birth optimization (closing the cycle) and H_0 death optimization (keeping the point cloud connected) on macrocycle generation, both in the unconditional and conditional setting. We keep the H_1 death optimization unchanged, as it is the core of the method. We generate sets of 1000 molecules with MolDiff+MACROGUIDE and MolSnapper+MACROGUIDE, and report results in Table 6 and Table 7 respectively.

We observe a drop in macrocycle generation when the birth of the H_1 component is not constrained as this may lead to the creation of non-closed cycles. On the other hand, the lack of H_0 death term, while not detrimental to macrocycle generation performance or macrocycle quality, results in a drop in connected molecules and hence a drop in successfulness (Table 6).

In the protein conditioning setting, the lack of H_1 birth term produces a similar drop in performance. However, H_0 death optimization can be safely removed, probably because of the confined volume of the protein pocket (Table 7).

J.3 ABLATIONS OF SQUARES

We perform additional experiments with and without squaring the key equations in the topological loss. The results in Table 8 and Table 9 show that adding a square to H_1 birth decreases the rate

Table 6: **Ablations of different guidance terms in the unconditional setting.** The metrics most affected by the ablation are in bold. Some metrics are not reported because not enough successful macrocycles were produced. Results were obtained from sets of 1000 molecules.

Metrics (↑; [0-1])	MolDiff +MACROGUIDE (ours)	No H_1 birth	No H_0	No H_1 birth and no H_0
Validity	0.989	0.990	0.990	0.990
Connectivity	0.999	0.954	**0.863**	**0.022**
Successfulness	0.988	0.944	0.854	0.022
Out of successful:				
Macrocycles	0.997	**0.075**	0.995	**0.091**
Out of macrocycles:				
Diversity	0.771	0.735	0.774	-
Novelty	1.000	1.000	1.000	-
Uniqueness	1.000	1.000	1.000	-
All PoseBusters tests	0.805	0.732	0.840	-
Bond lengths	0.990	1.000	0.994	-
Bond angles	0.987	0.761	0.985	-
Internal steric clash	0.844	0.972	0.893	-
Aromatic ring flatness	0.999	1.000	1.000	-
Non-ar. ring non-flatness	0.999	1.000	1.000	-
Double bond flatness	0.989	1.000	0.968	-
Internal energy	0.984	1.000	0.991	-

Table 7: **Ablations of different guidance terms in the conditional setting.** The metrics most affected by the ablation are in bold. Some metrics are not reported because not enough successful macrocycles were produced. Results were obtained from sets of 1000 molecules.

Metrics (↑; [0-1])	MolSnapper +MACROGUIDE (ours)	No H_1 birth	No H_0	No H_1 birth and no H_0
Validity	0.925	0.903	0.921	0.929
Connectivity	1.000	1.000	1.000	1.000
Successfulness	0.925	0.903	0.921	0.929
Out of successful:				
Macrocycles	0.995	**0.078**	0.989	**0.016**
Out of macrocycles:				
Diversity	0.712	0.734	0.711	-
Novelty	1.000	1.000	1.000	-
Uniqueness	1.000	1.000	0.999	-
All PoseBusters tests	0.575	0.414	0.591	-
Ligand PoseBusters	0.626	0.471	0.654	-
Bond lengths	0.860	0.829	0.923	-
Bond angles	0.888	0.643	0.907	-
Internal steric clash	0.854	0.914	0.854	-
Aromatic ring flatness	0.992	0.986	0.993	-
Non-ar. ring non-flatness	0.999	1.000	1.000	-
Double bond flatness	0.993	0.986	0.995	-
Internal energy	0.921	0.929	0.926	-
Protein PoseBusters	0.911	0.843	0.902	-
Protein-ligand max. distance	1.000	1.000	1.000	-
Min. distance to protein	0.907	0.843	0.902	-
Volume overlap with protein	1.000	1.000	1.000	-
Pharmacophore satisfaction	0.789	0.829	0.804	-
Macrocycle Lipinski	0.638	0.743	0.580	-

of macrocycle generation, as well as their PoseBusters performance, both in the unconditional and conditional settings.

Omitting the H_1 death square results in a decrease in molecule validity and the PoseBusters checks performance for macrocycles. Finally, the lack of H_0 death square seems the least detrimental to

model performance, and even improves the performance for some metrics. This term modification can therefore act as a good starting point for adapting MACROGUIDE for specific tasks.

Table 8: **Influence of the square on each guidance term in the unconditional setting.** The metrics most affected by the ablation are in bold. Results were obtained from sets of 1000 molecules.

Metrics (↑; [0-1])	MolDiff +MACROGUIDE (ours)	+H_1 birth square	No H_1 death square	No H_0 death square
Validity	0.989	0.981	**0.924**	0.991
Connectivity	0.999	0.985	1.000	1.000
Successfulness	0.988	0.966	0.924	0.991
Out of successful:				
Macrocycles	0.997	**0.633**	0.998	1.000
Out of macrocycles:				
Diversity	0.771	0.789	0.782	0.752
Novelty	1.000	1.000	1.000	1.000
Uniqueness	1.000	1.000	1.000	1.000
All PoseBusters tests	0.805	**0.628**	**0.711**	0.791
Bond lengths	0.990	0.964	0.935	0.989
Bond angles	0.987	0.702	0.938	0.987
Internal steric clash	0.844	0.913	0.837	0.815
Aromatic ring flatness	0.999	0.998	0.999	0.996
Non-ar. ring non-flatness	0.999	0.998	0.999	0.996
Double bond flatness	0.989	0.987	0.977	0.987
Internal energy	0.984	0.959	0.953	0.987

Table 9: **Influence of the square on each guidance term in the conditional setting.** The metrics most affected by the ablation are in bold. Results were obtained from sets of 1000 molecules.

Metrics (↑; [0-1])	MolSnapper +MACROGUIDE (ours)	+H_1 birth square	No H_1 death square	No H_0 death square
Validity	0.925	0.914	**0.883**	0.915
Connectivity	1.000	1.000	1.000	1.000
Successfulness	0.925	0.914	0.883	0.915
Out of successful:				
Macrocycles	0.995	**0.521**	0.998	0.991
Out of macrocycles:				
Diversity	0.712	0.711	0.717	0.703
Novelty	1.000	1.000	1.000	1.000
Uniqueness	1.000	1.000	1.000	1.000
All PoseBusters tests	0.575	**0.309**	0.529	0.572
Ligand PoseBusters	0.626	0.332	0.580	0.607
Bond lengths	0.860	0.800	0.815	0.869
Bond angles	0.888	0.502	0.879	0.905
Internal steric clash	0.854	0.851	0.846	0.847
Aromatic ring flatness	0.992	0.987	0.993	0.981
Non-ar. ring non-flatness	0.999	1.000	1.000	1.000
Double bond flatness	0.993	0.989	0.992	0.999
Internal energy	0.921	0.905	0.910	0.899
Protein PoseBusters	0.911	0.891	0.915	0.940
Protein-ligand max. distance	1.000	1.000	1.000	1.000
Min. distance to protein	0.907	0.891	0.915	0.940
Volume overlap with protein	1.000	1.000	0.999	1.000
Pharmacophore satisfaction	0.789	0.824	0.820	0.744
Macrocycle Lipinski	0.638	0.670	0.640	0.630

J.4 GUIDANCE STRENGTH

Tables 10 and 11 demonstrate that the chosen guidance strength of 1 performs consistently well across both unconditional and conditional settings.

Table 10: **Influence of guidance strength on performance in the unconditional setting.** The original results from Table 3 correspond to the strength of 1. Results were obtained from 1000 samples.

Metrics (↑; [0-1])	0.1	0.5	MolDiff +MACROGUIDE 1.0 (ours)	1.5	2.0
Validity	0.994	0.995	0.989	0.991	0.992
Connectivity	0.999	0.996	0.999	0.996	0.988
Successfulness	0.993	0.991	0.988	0.987	0.980
Out of successful:					
Macrocycles	0.769	0.967	0.997	0.990	0.754
Out of macrocycles:					
Diversity	0.752	0.763	0.771	0.780	0.796
Novelty	1.000	1.000	1.000	1.000	1.000
Uniqueness	1.000	0.999	1.000	0.992	1.000
All PoseBusters tests	0.662	0.754	0.805	0.870	0.548
Bond lengths	0.986	0.996	0.990	0.997	0.961
Bond angles	0.808	0.947	0.987	0.939	0.608
Internal steric clash	0.823	0.813	0.844	0.960	0.963
Aromatic ring flatness	0.992	0.997	0.999	1.000	1.000
Non-ar. ring non-flatness	0.995	0.997	0.999	0.999	1.000
Double bond flatness	0.986	0.990	0.989	0.990	0.991
Internal energy	0.976	0.977	0.984	0.975	0.951

Table 11: **Influence of guidance strength on performance in the conditional setting.** The original results from Table 3 correspond to the strength of 1. Results were obtained from 1000 samples.

Metrics (↑; [0-1])	0.1	0.5	MolSnapper +MACROGUIDE 1.0 (ours)	1.5	2.0
Validity	0.924	0.933	0.925	0.876	0.891
Connectivity	1.000	1.000	1.000	1.000	1.000
Successfulness	0.924	0.933	0.925	0.876	0.891
Out of successful:					
Macrocycles	0.411	0.867	0.995	0.995	0.845
Out of macrocycles:					
Diversity	0.655	0.695	0.712	0.724	0.724
Novelty	1.000	1.000	1.000	1.000	1.000
Uniqueness	1.000	1.000	1.000	1.000	1.000
All PoseBusters tests	0.384	0.507	0.575	0.495	0.154
Ligand PoseBusters	0.426	0.561	0.626	0.561	0.206
Bond lengths	0.876	0.890	0.860	0.854	0.789
Bond angles	0.658	0.791	0.888	0.802	0.311
Internal steric clash	0.824	0.847	0.854	0.874	0.870
Aromatic ring flatness	0.995	0.994	0.992	0.987	0.991
Non-ar. ring non-flatness	1.000	0.999	0.999	0.999	0.999
Double bond flatness	0.982	0.984	0.993	0.993	0.985
Internal energy	0.876	0.927	0.921	0.911	0.902
Protein PoseBusters	0.895	0.886	0.911	0.857	0.744
Protein-ligand max. distance	1.000	1.000	1.000	1.000	1.000
Min. distance to protein	0.895	0.886	0.907	0.857	0.744
Volume overlap with protein	1.000	1.000	1.000	1.000	0.993
Pharmacophore satisfaction	0.800	0.808	0.789	0.828	0.838
Macrocycle Lipinski	0.603	0.642	0.638	0.673	0.659

J.5 ATOM TYPE DISTRIBUTION

Table 12 reports the distribution of atom types in the generated macrocycles.

Table 12: **Atom distribution of generated macrocycles.** Represented as a fraction of all atoms.

Method	C	N	O	F	P	S	Cl
MolDiff (no guid.)	0.7978	0.0798	0.1089	0.0011	0.0000	0.0113	0.0011
+MACROGUIDE (ours)	0.8785	0.0477	0.0722	0.0001	0.0000	0.0014	0.0001
MolSnapper (no guid.)	0.7508	0.1749	0.0714	0.0002	0.0000	0.0024	0.0003
+MACROGUIDE (ours)	0.7540	0.1921	0.0483	0.0000	0.0000	0.0051	0.0005

J.6 RING SIZE DISTRIBUTION

Table 13 reports the number of small rings present in the generated molecules. Generated macrocycles typically contain a few additional rings, indicating that they are not merely simple large cycles but exhibit nontrivial structural complexity. Moreover, MACROGUIDE reduces the number of 3- and 4-membered rings, which are the most strained and therefore undesirable, leading to chemically more favourable structures.

Table 13: **Ring size distribution in generated macrocycles.** Represented as the average number of cycles of a certain size per molecule.

Method	3-cycles (↓)	4-cycles (↓)	5-cycles	6-cycles	7-cycles	8-cycles	9-cycles
MolDiff (no guid.)	0.054	0.022	0.482	2.552	0.154	0.022	1.885
+MACROGUIDE (ours)	0.065	0.022	0.449	1.933	0.033	0.003	1.229
MolSnapper (no guid.)	0.258	0.082	1.005	2.919	0.133	0.009	2.216
+MACROGUIDE (ours)	0.183	0.077	1.123	2.127	0.039	0.001	1.341

J.7 RUNTIME COMPARISON

J.7.1 APPLYING GUIDANCE EVERY FEW STEPS

To reduce computational cost, the topological guidance can be applied only every few denoising iterations. Table 14 shows that applying MACROGUIDE once every up to 5 steps results in only a slight degradation of the performances, while substantially decreasing the overall computational overhead.

J.7.2 STARTING TOPOLOGICAL GUIDANCE LATE

Table 15 analyzes the effect of delaying the onset of topological guidance. The guidance can be introduced halfway through the denoising process with minimal impact on molecular validity, macrocycle-related metrics, and PoseBusters performance.

Table 14: **Performance of protein-conditioned macrocycle generation with guidance applied every few steps.** The first two columns correspond to Table 3. Values outperforming or matching the baseline MolSnapper metrics are in bold.

Metrics (↑; [0-1])	MolSnapper (no guid.)	Every 1	Every 2	Every 3	Every 4	Every 5
Validity	0.858	**0.925**	**0.930**	**0.942**	**0.914**	**0.940**
Connectivity	1.000	**1.000**	**1.000**	**1.000**	**1.000**	**1.000**
Successfulness	0.858	**0.925**	**0.930**	**0.942**	**0.914**	**0.940**
Out of successful:						
Macrocycles	0.003	**0.995**	**0.943**	**0.911**	**0.864**	**0.852**
Out of macrocycles:						
Diversity	0.626	**0.712**	**0.709**	**0.713**	**0.711**	**0.723**
Novelty	1.000	**1.000**	**1.000**	**1.000**	**1.000**	**1.000**
Uniqueness	1.000	**1.000**	**1.000**	**1.000**	**1.000**	**1.000**
All PoseBusters tests	0.440	**0.575**	**0.590**	**0.569**	**0.535**	**0.503**
Ligand PoseBusters	0.539	**0.626**	**0.658**	**0.661**	**0.637**	**0.624**
Bond lengths	0.844	**0.860**	**0.900**	**0.927**	**0.925**	**0.928**
Bond angles	0.913	0.888	**0.918**	**0.916**	0.890	0.850
Internal steric clash	0.862	0.854	0.856	0.851	0.839	**0.869**
Aromatic ring flatness	0.996	0.992	0.995	0.994	**0.997**	0.990
Non-ar. ring non-flatness	0.993	**0.999**	**1.000**	**0.999**	**0.999**	**1.000**
Double bond flatness	0.980	**0.993**	**0.992**	**0.986**	**0.985**	**0.983**
Internal energy	0.818	**0.921**	**0.928**	**0.920**	**0.916**	**0.920**
Protein PoseBusters	0.806	**0.911**	**0.895**	**0.875**	**0.838**	0.792
Protein-ligand max. distance	1.000	**1.000**	**1.000**	**1.000**	**1.000**	**1.000**
Min. distance to protein	0.806	**0.907**	**0.895**	**0.875**	**0.838**	0.792
Volume overlap with protein	1.000	**1.000**	**1.000**	**1.000**	**1.000**	0.999
Pharmacophore satisfaction	0.769	**0.789**	**0.791**	**0.800**	**0.820**	**0.823**
Macrocycle Lipinski	0.551	**0.638**	**0.692**	**0.698**	**0.682**	**0.693**

Table 15: **Performance of protein-conditioned macrocycle generation with guidance starting late.** The number denotes the number of remaining denoising steps when the guidance is applied, out of 1000 steps total. The first two columns correspond to Table 3. Values outperforming or matching the baseline MolSnapper metrics are in bold. Non-baseline results were obtained from sets of 200 molecules.

Metrics (↑; [0-1])	MolSnapper (no guid.)	1000 steps	900 steps	800 steps	700 steps	600 steps	500 steps	400 steps	300 steps	200 steps	100 steps
Validity	0.858	**0.925**	**0.925**	**0.925**	**0.910**	**0.920**	**0.940**	**0.905**	**0.910**	**0.860**	0.840
Connectivity	1.000	**1.000**	**1.000**	**1.000**	**1.000**	**1.000**	**1.000**	**1.000**	**1.000**	**1.000**	**1.000**
Successfulness	0.858	**0.925**	**0.925**	**0.925**	**0.910**	**0.920**	**0.940**	**0.905**	**0.910**	**0.860**	0.840
Out of successful:											
Macrocycles	0.003	**0.995**	**0.995**	**0.989**	**0.984**	**0.995**	**0.995**	**1.000**	**0.995**	**0.965**	**0.935**
Out of macrocycles:											
Diversity	0.626	**0.712**	**0.711**	**0.698**	**0.695**	**0.672**	**0.686**	**0.676**	**0.670**	**0.672**	**0.704**
Novelty	1.000	**1.000**	**1.000**	**1.000**	**1.000**	**1.000**	**1.000**	**1.000**	**1.000**	**1.000**	**1.000**
Uniqueness	1.000	**1.000**	**1.000**	**1.000**	**1.000**	**1.000**	**1.000**	**1.000**	**1.000**	**1.000**	**1.000**
All PoseBusters tests	0.440	**0.575**	**0.598**	**0.552**	**0.547**	**0.503**	**0.551**	**0.486**	0.376	0.319	0.178
Ligand PoseBusters	0.539	**0.626**	**0.658**	**0.623**	**0.654**	**0.601**	**0.684**	**0.652**	**0.547**	0.446	0.306
Bond lengths	0.844	**0.860**	**0.880**	**0.869**	**0.922**	**0.863**	**0.914**	**0.884**	**0.917**	**0.886**	0.834
Bond angles	0.913	0.888	0.902	0.852	**0.927**	0.902	0.888	**0.923**	0.834	0.789	0.561
Internal steric clash	0.862	0.854	**0.864**	**0.896**	0.855	0.814	**0.877**	**0.873**	**0.890**	0.813	0.841
Aromatic ring flatness	0.996	0.992	**1.000**	**1.000**	0.994	**1.000**	0.995	0.994	0.994	**1.000**	**1.000**
Non-ar. ring non-flat.	0.993	**0.999**	1.000	**1.000**	**1.000**	**1.000**	0.995	**1.000**	**1.000**	**1.000**	**1.000**
Double bond flatness	0.980	**0.993**	**0.995**	**0.989**	**0.994**	**0.995**	**0.989**	**0.989**	0.961	0.910	0.930
Internal energy	0.818	**0.921**	**0.929**	**0.951**	**0.894**	**0.891**	**0.925**	**0.923**	0.796	**0.867**	**0.822**
Protein PoseBusters	0.806	**0.911**	**0.913**	**0.902**	**0.844**	**0.852**	0.786	0.790	0.740	0.765	0.561
Prot.-ligand max. dist.	1.000	**1.000**	**1.000**	**1.000**	**1.000**	**1.000**	**1.000**	**1.000**	**1.000**	**1.000**	**1.000**
Min. dist. to protein	0.806	**0.907**	**0.913**	**0.902**	**0.844**	**0.852**	0.786	0.790	0.740	0.765	0.561
Vol. overlap with prot.	1.000	**1.000**	**1.000**	**1.000**	**1.000**	**1.000**	**1.000**	**1.000**	**1.000**	**1.000**	**1.000**
Pharmacophore satisfaction	0.769	**0.789**	**0.804**	**0.809**	**0.816**	**0.820**	**0.893**	**0.823**	**0.818**	**0.819**	**0.815**
Macrocycle Lipinski	0.551	**0.638**	**0.598**	**0.639**	**0.598**	**0.557**	**0.620**	**0.602**	**0.713**	**0.669**	**0.732**

K INTEGRATING BOND-LEVEL INFORMATION: CHALLENGES

The following strategies have been tested in order to integrate bond-level information in our macrocycle guidance function.

1. Maximizing the H_1 component **death edge probability** in our method.
2. Computing a **representative cycle** of our H_1 component. However this task is both computationally expensive and ambiguous, as a representative cycle is not unique.
3. Pre-selecting the **ordered set of atoms** to form the cycle (before sampling), and maximizing edge probabilities while minimizing chord probabilities.
4. Pre-selecting the **unordered set of atoms** to form the cycle (before sampling), and applying H_1 guidance on this subset during sampling based on distances computed from probabilities.

None of the attempts mentioned yield convincing results, which we explain with the following three reasons. First, MACROGUIDE already achieves a 99% macrocycle rate without integrating bond information. Consequently one can hardly hope for significant improvements. Second, any minimization of a chord probability is challenged by the fact that minimizing the probability of a bond can be done both by pushing the atoms apart and by bringing them very close, without a clear way to choose which one. Third, any backpropagation of the bond-predictor model is much more computationally expensive than our current guidance, as well as relying on the quality and robustness of this model. As a consequence, we believe that trying further to integrate bond-level information is not a priority.